Stony Brook University

OFFICIAL COPY

The official electronic file of this thesis or dissertation is maintained by the University Libraries on behalf of The Graduate School at Stony Brook University.

© All Rights Reserved by Author.

Studies on the Synthesis of Gallium Nitride Nanostructures by Chemical Vapor Deposition at Low Temperatures and Stress Analysis for Multicrystalline Silicon for Solar Cells

A Thesis Presented

by

Christopher Yee Ping Chow

to

The Graduate School

in Partial Fulfillment of the

Requirements

for the Degree of

Master of Science

in

Chemistry

Stony Brook University

August 2008

Stony Brook University

The Graduate School

Christopher Yee Ping Chow

We, the thesis committee for the above candidate for the

Master of Science degree, hereby recommend

acceptance of this thesis.

Michael Dudley – Thesis Advisor
Professor, Department of Materials Science and Engineering

Joseph W. Lauher - Chairperson of Defense
Professor, Department of Chemistry

Balaji Raghothamachar
Research Assistant Professor, Department of Materials Science and Engineering

Peter Khalifah
Assistant Professor, Department of Chemistry

This thesis is accepted by the Graduate School

Lawrence Martin
Dean of the Graduate School

Abstract of the Thesis

Studies on the Synthesis of Gallium Nitride Nanostructures by Chemical Vapor Deposition at Low Temperatures and Stress Analysis for Multicrystalline Silicon for Solar Cells

by

Christopher Yee Ping Chow

Master of Science

in

Chemistry

Stony Brook University

2008

Solid state lighting and photovoltaic (chiefly, solar) technologies are increasingly being sought to reduce energy costs and provide alternative sources of energy, respectively. Gallium nitride (GaN) is a wide bandgap semiconductor that emits light in the UV range and is steadily replacing traditional semiconductors such as GaAs and GaP in many applications. Although much progress has been made on bulk GaN and its application in optoelectronic devices, research on growing GaN in the nanoscale, in particular one-dimensional (1-D) nanostructures has been gaining interest primarily due to its novel physical properties that depend on its size and dimensionality. Silicon, chiefly in multicrystalline form, is the material primarily used for fabricating solar cells that typically have efficiencies between 15-20%. The recent heavy demand for silicon solar cells has created a shortage of silicon and has necessitated modifications to the current manufacturing process to improve yield and minimize loss of material significantly.

The following studies have been carried out:

I. The low temperature CVD growth of GaN nanostructures on boron nitride (BN) substrates was investigated under both non-catalytic and catalytic environments (Ni catalyst, UV radiation). Gallium acetylacetonate and, a powdered mixture of Ga and calcium fluoride (CaF_2) were used as gallium precursors to react with ammonia (NH_3) gas. Various NH_3 flow rates and chamber pressures were used at different temperatures. The morphologies and crystal structure were characterized using scanning electron microscopy with energy dispersion X-ray spectrospcopy, and transmission electron microscopy. With the use of a Ni catalyst, GaN nanopowders has been grown at temperatures as low as 400 ^{o}C. GaN nanoneedles were grown at 75 sccm flow rate with 15 torr pressure. A high density of nanoneedles was observed with the assistance of UV radiation.

II. The stress distribution on the surfaces of band-sawed mc-Si bricks and wire-sliced wafers from the bricks processed to different stages of the solar cell fabrication process has been investigated. The procedure characterizing its grain structure, strain level and dislocation content of mc-Si at each stage of the processing sequence was carried out by using the technique of synchrotron white beam X-ray topography (SWBXT). Quantitative information on shear stress is obtained by employing the technique of synchrotron white beam X-ray reticulography (SWBXR). Results indicate that the mc-Si brick has variation of shear stress along the four faces that are possibly caused by non-uniform cooling after growth. As for the sets of wafers processed in various stages for solar cell fabrication, the print wafer showed significant levels of stress at the metallic contacts.

Table of Contents

List of Acronyms vi

List of Symbols vii

List of Figures viii

List of Tables x

Acknowledgements xi

1. Low temperature CVD growth of GaN nanostructures 1

1.1 Introduction 1
1.1.1 Structural and electrical properties of GaN 1
1.1.2 Thermodynamic properties of GaN 3
1.1.3 Thermodynamics and spectroscopic properties on the decomposition of NH_3 3
1.1.4 Substrate requirements to grow high quality GaN 5
1.1.5 Functional GaN nanostructures 6
1.1.5.1 Motivation 9

1.2 Experimental Method 10

1.3 Results & Discussion 13
1.3.1 GaN growth without the use of a metal catalyst 13
1.3.2 GaN growth with the use of a metal catalyst 17
1.3.3 UV-assisted GaN growth 19
1.3.4 Growth using powdered mixture of Ga and CaF_2 21

1.4 Conclusion 22

2. Stress Analysis of Multicrystalline Silicon for Solar Cells 24

2.1 Introduction 24
2.1.1 Crystal growth techniques for mc-Si 25
2.1.2 Wafer processing – Solar cell fabrication 25

2.2 Motivation 26

2.3 Experimental 26
2.3.1 Synchrotron X-ray Topography 27
2.3.2 Synchrotron X-ray Reticulography 29
2.3.3 Principle of strain/stress measurements using SWBXT 29
2.3.3.1 Shear strain/stress mapping procedure 30

2.4 Results & Discussion 31
2.4.1 SWBXR of Brick Faces 31
2.4.2 SWBXR of Wafers 36

2.4 Conclusion 42

3. Conclusions 43

Appendix - Chemical & Physical Properties of Gallium Acetylacetonate 44

References 46

List of Acronyms

CVD	chemical vapor deposition
TEM	transmission electron microscopy
HRTEM	high resolution transmission electron microscopy
SEM	scanning electron microscopy
SWBXT	synchrotron white beam X-ray topography
SWBXR	synchrotron white beam X-ray reticulography

List of Symbols

σ	stress (GPa)
ε	strain
(*hkil*)	Miller indices
[*hkil*]	unit cell direction
λ	wavelength (nm)

List of Figures

Figure 1. Comparison of band gaps between III-Nitrides & traditional compound semiconductors with the corresponding energy spectrum. As illustrated, GaAs has a band gap that can emit light in the IR range and GaP in the green wavelength. 1

Figure 2. $(11\bar{2}0)$ projection of (a) wurtzite and $(10\bar{1})$ projection of (b) zinc-blende GaN. Large and small atoms denotes Ga and N respectively. The stacking sequences are “ABAB…” and “ABCABC…” for wurtzite and zinc-blende GaN respectively. 2

Figure 3. Phase diagram of the Ga-N system under 1 bar N_2. X_N denotes the molar fraction of nitrogen. Beyond temperatures of 1117 ^oK (844 ^oC), GaN growth is unfeasible and is decomposed to liquid and gas phases. 3

Figure 4. Lewis structures of (a) NH_3 and (b) N_2 revealing its bonding nature and is indicative of the bond dissociation energies. 4

Figure 5. Absorption spectrum of NH_3 decomposition at various wavelengths as a function of temperature. 5

Figure 6. Nanowire growth by the VLS mechanism using the bottom-up approach. A droplet of metal alloy is formed (a) on the substrate from the vapor and acts as a catalyst dictating the axial growth of (b) the nanowire. 7

Figure 7. Binary Ni-Ga phase diagram which there are six phases indicating incongruent melting and NiGa being the only solid solution forms congruently. NiGa is stable at 950 ^oC with Ga at. % ranging from 35 to 50%. 8

Figure 8. Isothermal ternary Ni-Ga-N phase diagram at 500 ^oC at 1 bar of pressure. 8

Figure 10. CVD setup using UV-assisted beam 11

Figure 11. Growth setup using Ga and CaF_2 mixed in powdered form. 11

Figure 12. Temperature distribution along the length of the quartz tube at several growth temperatures 12

Figure 13. SEM image (a) and the EDX spectrum (b) of the GaN matrix grown at 650 ^oC with NH_3 = 100 sccm and p = 200 torr in 160 min. 13

Figure 14. SEM image (a) and EDX spectrum (b) of clumped GaN nanoparticles grown at 500 ^oC with NH_3 = 100 sccm and p = 200 torr in 130 min. 14

Figure 15. TEM images projected along $[1\bar{1}00]$ of the nanoneedle grown at 450 ^oC with NH_3 = 75 sccm and p = 15 torr in 90 mins. (a) TEM image showing the full length of the nanoneedle and, (b) the diameter. (c) HRTEM image showing the lattice spacing. (d)-(e) HRTEM images of regions 1 and 2 indicated by the broken line box in (a) respectively; the inset denotes the partial edge dislocation indicated by the white box. 16

Figure 16. SEM image (a) and EDX spectrum (b) of clumped GaN nanoparticles grown via Ni catalyst at 500 ^oC (NH_3 = 100 sccm, p = 200 torr) in 130 min. The nanoparticle size estimates from 75 ~ 90 nm. 17

Figure 17. SEM image (a) and EDX spectrum with the corresponding SAED pattern inset (b) of clumped GaN nanoparticles grown via Ni catalyst at 450 ^oC (NH_3 = 100 sccm, p = 35 torr) in 120 min. The nanoparticle size ranges from 100 ~ 130 nm. 18

Figure 18. SEM image (a) EDX spectrum with the corresponding SAED pattern inset (b) and (c) TEM image of GaN porous platelets grown via Ni catalyst at 400 ^oC (NH_3 = 100 torr, p = 20 torr) in 240 min... 19

Figure 19. SEM image (a) and, HRTEM images projected along $[1\bar{1}00]$ (b) showing the lattice spacing and (c)-(d) of GaN nanoneedles grown at 600 ^oC illustrating the diameters of the nanoneedles and confirming its crystal structure. 20

Figure 20. (a) SEM image of stem-like nanoneedles grown at 450 ^{o}C. (b) HRTEM showing the interplanar spacing and (c) low-magnification TEM indicating the diameter of the nanoneedle of 32 nm....................21

Figure 21. (a) SEM micrograph of the CaF_2 particle. (b) SEM image of (a) under high magnification illustrating the CaF_2 crystallites. (c) EDX spectrum of (b)...22

Figure 22. Representation of a *p-n* junction solar cell illustrating the carrier generation from the interaction of photons, E_v is the valence band energy, E_f is the Fermi energy and E_c is the conduction band energy. ...24

Figure 23. Schematic representation of both ingot and sheet techniques. (a) Bridgman technique, (b) Heat extraction method (HEM), (c) Electromagnetic casting (EMC) technique, (d) Edge-defined-film-fed-growth (EFG) sheet technique. 25

Figure 24. Schematic representation of a solar cell with titanium oxide (TiO_x) as an ARC and, printing of front and back Al contacts. 26

Figure 25. Recording geometries for synchrotron white beam X-ray topography / reticulography (a) Reflection geometry employed for recording topographs and reticulographs from surface of mc-Si brick; (b) Transmission geometry employed for wafers recording topographs and reticulographs from wafers (Note: Grating is employed only during recording of reticulographs). 27

Figure 26. Orientation contast arising from misoriented regions: (a) monochromatic radiation (beam divergence < misorientation); (b) monochromatic radiation (beam divergence > misorientation); and (c) continuous radiation (e.g. synchrotron white beam) 28

Figure 27. Schematic for synchrotron white beam X-ray reticulography (SWBXR) measurements. 29

Figure 28. (a) Tilting of lattice planes due to simple shear; (b) Orientation contrast due to tilt (Note: Magnitude of angle α with respect to the Bragg angle θ_B is exaggerated. $\alpha << \theta_B$. Also the sample-film distance L is very large (~ 300mm) compared to ΔS)..30

Figure 29. X-ray Reticulograph taken from one section of Face 4...31

Figure 30. Schematic and notation of measuring distortion 31

Figure 31. Schematic of brick sample 32

Figure 32. X-ray images of the four faces of mc-Si brick assembled from reticulographs of various grains. *Note*: First-to-solidify end is to the left and the last-to-solidify end is to the right in each figure. 34

Figure 33. Stress map of four faces of the mc-Si brick sample from the corresponding reticulographs in figure 32. 36

Figure 34. Optical photographs of wafers sliced from the brick sample and processed to different stages of the solar cell fabrication. Black rectangle denotes region containing small grains. These grains are slightly misoriented with respect to main wafer orientation. 37

Figure 35. X-ray reticulographs and its corresponding stress maps of wafers sliced from the brick sample and processed to different stages of the solar cell fabrication. 41

Figure 36. Line structure (a) and (b) the ball and stick model of $Ga(acac)_3$ showing its atomic numbering.45

List of Tables

Table 1. Band gap comparison between III-Nitrides & GaAs, GaP 1
Table 2. Lattice & thermal properties between GaN and its substrates 6
Table 3. List of wafers studied 37
Table 4. Bond lengths & angles of gallium (III) acetylacetonate 44

Acknowledgements

First I would like to give my sincere gratitude to Prof. Michael Dudley, for giving me an opportunity to work in the crystal growth and characterization field. I also want to give my sincere appreciation to Dr. Balaji Raghothamachar for his wide knowledge, helpful mentoring and encouragement during my graduate studies. Without a doubt, both Prof. Dudley and Dr. Raghothamachar have assisted me in landing a great post-graduate career opportunity.

Second, I would like to thank my family; my brother Steve for being a consummate role-model and friend and, my parents for making sacrifices throughout my life.

I also owe Dr. Joan Carvajal for his informative discussion on the experimental and results regarding GaN nanostructures.

I would like to thank Prof. Joseph W. Lauher and Prof. Peter Khalifah for being my thesis committee members and their valuable advice.

I would also want to thank my colleagues: Dr. Yi Chen, Dr. Guan Wang, Ms. Hui Chen, Mr. Ning Zhang, Mr. Vish Sarkar, and Ms. Yu Zhang for their valuable support during my research.

This work is supported by the National Science Foundation (NSF) under award number CBET-0617760. HRTEM work was carried out on the JEOL FEM 3000F and 2100F electron microscope at the Center for Functional Nanomaterials (CFN), Brookhaven National Laboratory, which is supported by the U.S. Department of Energy, Division of Materials Sciences and Division of Chemical Sciences, under Contract No. DE-AC02-98CH10886. Topography experiments were carried out at the Stony Brook Synchrotron Topography Facility, Beamline X-19C, at the NSLS (Contract no. DE-AC02-76CH00016).

1. Low temperature CVD growth of GaN nanostructures

1.1 Introduction

1.1.1 Structural and electrical properties of GaN

Gallium nitride (GaN), aluminum nitride (AlN) and indium nitride (InN) are III-nitride semiconductors that exhibits a wide band gap which has great potential in developing applications from the infrared (IR) to UV. The III-nitrides are steadily replacing traditional semiconductors such as GaAs and GaP, only emitting at the IR and green wavelengths respectively. Table 1 shows the comparison of band gaps between the III-nitrides and other compound semiconductors (e.g. GaAs and GaP) and figure 1 shows the comparison of band gaps between the III-nitrides with its alloys and various semiconductors with the corresponding energy spectrum.

Table 1. Band gap comparison between III-Nitrides & GaAs, GaP

	Band Gap E_g (eV)
GaN	3.4
AlN	6.2
InN	0.7
GaAs	1.4
GaP	2.3

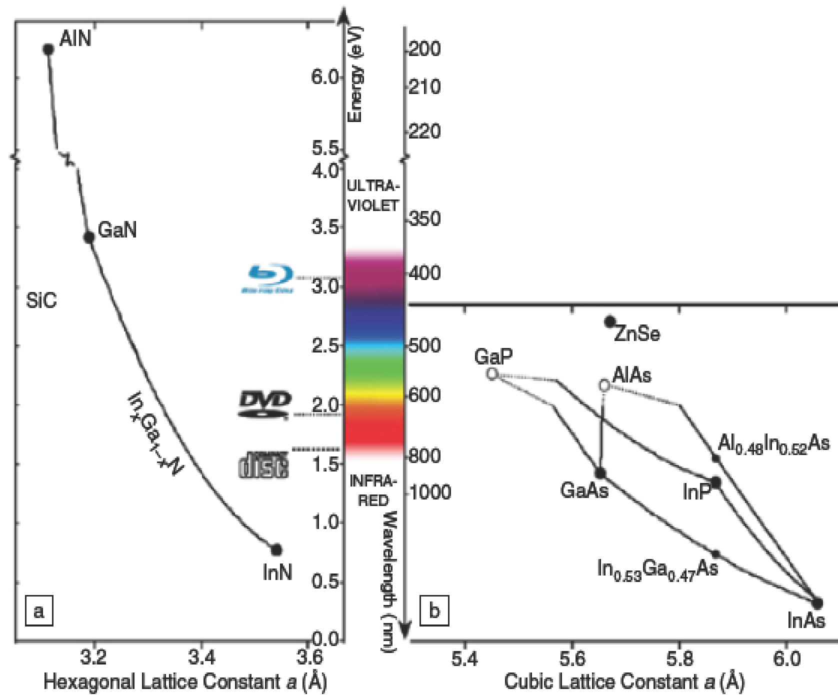

Figure 1. Comparison of band gaps between III-Nitrides & traditional compound semiconductors with the corresponding energy spectrum[1]. As illustrated, GaAs has a band gap that can emit light in the IR range and GaP in the green wavelength.

As shown in figure 1, the advantages of GaN is that it can alloy with AlN and indium nitride (InN) forming $In_xGa_{1-x}N$, which is useful in fabricating devices from the near-IR to near-UV and $Al_xGa_{1-x}N$, emiting light in the deep-UV hence has practical applications in water splitting and biosensors. The III-nitrides also have a direct band gap which has an advantage over indirect band gap semiconductors where momentum is required to excite an electron to its conduction band and this is normally supplied by a phonon, which is a quantized lattice vibration to aid in the process[2] thus some energy is lost at emitting light.

GaN has two polytypes[3], the hexagonal wurtzite with lattice parameters of a = 3.189 Å and c = 5.185 Å which has a stacking sequence of "ABABAB…" and, cubic zinc-blende having a lattice parameter of 4.5 Å with stacking sequence of "ABCABCABC…". Figure 2 illustrates both $(11\bar{2}0)$ of wurtzite and $(10\bar{1})$ projections of zinc-blende GaN structures.

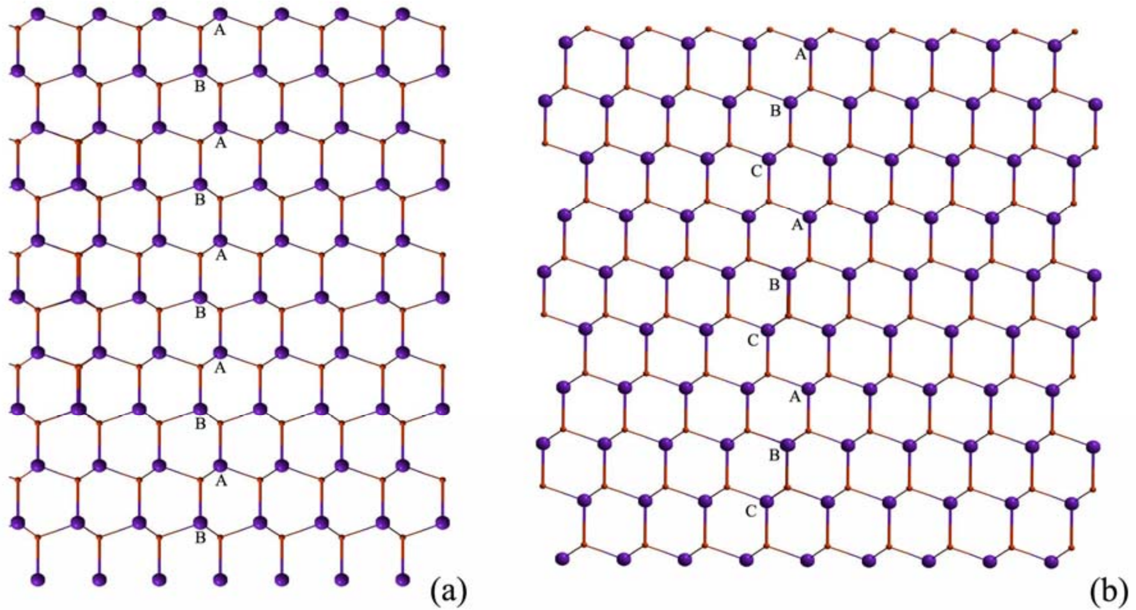

Figure 2. $(11\bar{2}0)$ projection of (a) wurtzite and $(10\bar{1})$ projection of (b) zinc-blende GaN. Large and small atoms denotes Ga and N respectively. The stacking sequences are "ABAB…" and "ABCABC…" for wurtzite and zinc-blende GaN respectively.

The wurtzite polytype is thermodynamically stable than the zinc-blende polytype in which the majority of the zinc-blende GaN has been synthesized on various cubic[3] substrates such as Si(001) and GaAs under nonequilibrium conditions. The reason for the interest of obtaining a cubic GaN crystal structure is due to the suitability[4] of *n* or *p*-type doping based on similar lattice parameters. Growing GaN usually results with a high background of *n*-type carrier concentration (that is electrons are the majority carriers) due to point defects caused by nitrogen vacancies. Reducing the *n*-type background and introducing a *p*-type dopant to grow *p*-type GaN (where holes are the majority carriers) has been an ongoing area of research to improve the quality and efficiency of light emitting diodes (LEDs). The current problem of introducing a *p*-type impurity is the increase of resistivity causing the inability to facilitate conduction. Several workers[3] have

doped GaN with Zn and Mg resulting in reduction in *n*-type concentration and increasing *p*-type conductivity.

1.1.2 Thermodynamic properties of GaN

Thermodynamically, GaN is unstable at high temperatures and tends to decompose[5,6] around 800 ^{o}C. GaN is decomposed into the following elements

$$GaN(s) = Ga(l) + \frac{1}{2}N_2(g) \qquad [1.1]$$

It is essential to consider the phase diagram of GaN before carrying out growth. Figure 3 shows the phase diagram of the Ga-N system under 1 bar of nitrogen; when the system is beyond 800 ^{o}C (1073 ^{o}K), GaN decomposes to liquid and gas phases of Ga and N mixtures.

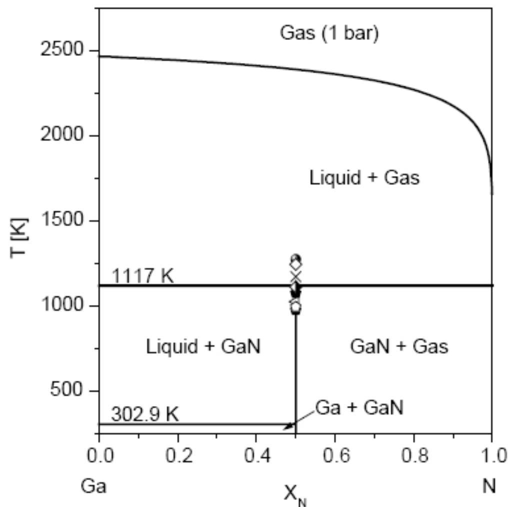

Figure 3. Phase diagram of the Ga-N system under 1 bar N_2.[7] X_N denotes the molar fraction of nitrogen. Beyond temperatures of 1117 ^{o}K (844 ^{o}C), GaN growth is unfeasible and is decomposed to liquid and gas phases.

1.1.3 Thermodynamics and spectroscopic properties on the decomposition of NH_3

The most common technique to grow GaN is the chemical vapor deposition (CVD) technique, which involves a chemical reaction of metallic Ga or GaCl and $Ga(CH_3)_3$ as Ga precursors under the presence of ammonia (NH_3) gas as a source of nitrogen. The deposition reaction of the formation of GaN when Ga is directly reacted with NH_3 is

$$Ga(s) + NH_3(g) = GaN(s) + \frac{3}{2}H_2(g) \qquad [1.2]$$

NH_3 is the acting source of nitrogen due to its single bonding nature of N–H and that it is unstable at high temperatures whereas N_2 has a triple bond and has high bond

dissociation energy. Figure 4 shows Lewis structures illustrating the bonding nature of both NH_3 and N_2 which indicates the significant difference of bond energies.

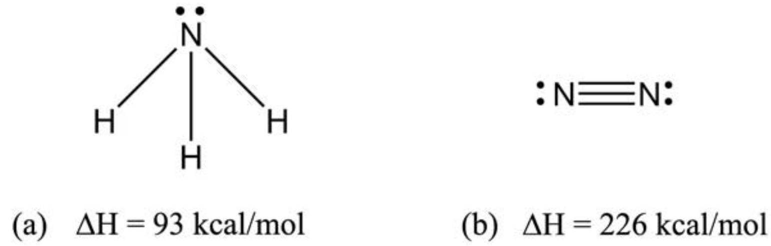

Figure 4. Lewis structures of (a) NH_3 and (b) N_2 revealing its bonding nature and is indicative of the bond dissociation energies.

It is crucial to take note of how much ammonia is decomposed, accordingly to the reaction

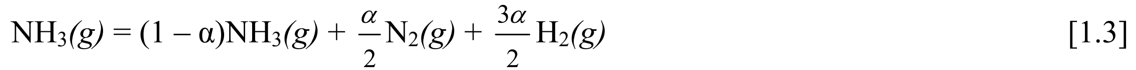

$$NH_3(g) = (1 - \alpha)NH_3(g) + \frac{\alpha}{2}N_2(g) + \frac{3\alpha}{2}H_2(g) \qquad [1.3]$$

where α is the degree of dissociation and is dependent on the effects of temperature, duration of reaction, and the catalytic environment in the reaction zone. The types of catalytic environments that initiate the decomposition of NH_3 are the use of a metal catalyst[8] such as Au, In, Fe, and Ni and, decomposition by UV-visible spectroscopy[9,10]. Liu[5] has found that NH_3 decomposes almost completely at 1150 ^oC with the presence of a Fe catalyst when carrying out CVD growth of GaN. There are several studies done on the thermal decomposition of NH_3 using a Ni catalyst. Chrysostomou *et al.*[11] has pointed out that transition metals are energetic towards the decomposition of NH_3. They have studied the thermal decomposition of ammonia adsorbed the surface of Ni(110) and found that NH_3 decomposes at 400 ^oK (127 ^oC) and 800 ^oK (527 ^oC) under the presence of H_2 and N_2 gases respectively. They have taken into account the stepwise hydrogenation-dehydrogenation[11] of ammonia

$$NH_{3,ads} \leftrightarrow NH_{2,ads} \rightarrow NH_{ads} \rightarrow N_{ads} \qquad [1.4]$$

that both NH_2 and NH are the reaction intermediates which can recombine with H to reform NH_3 and dehydrogenate to N respectively. Tamaru *et al.*[12] utilized a Ni catalyst by reducing nickel oxide and finds that NH_3 decomposes at 300 ^oC. They proposed that the amount of nitrogen adsorbed is based on the equilibrium constant K_p = $p_{NH_3} / \sqrt{p_{H_2}}$ from the reaction $NH_3(g) = NH_2 + ½ H_2(g)$ with NH_2 being the dominant species (and the remaining species, NH) for the adsorption of N.

Dietz *et al.*[13] has studied the decomposition of NH_3 UV absorption spectroscopy. As seen in figure 5, the amplitude increases with increasing temperature due to the variation in the absorption cross section and the absorption decreases at temperatures beyond 1000 K. The same trend occurs with increasing wavelengths with shifts of decreased absorption peak amplitude.

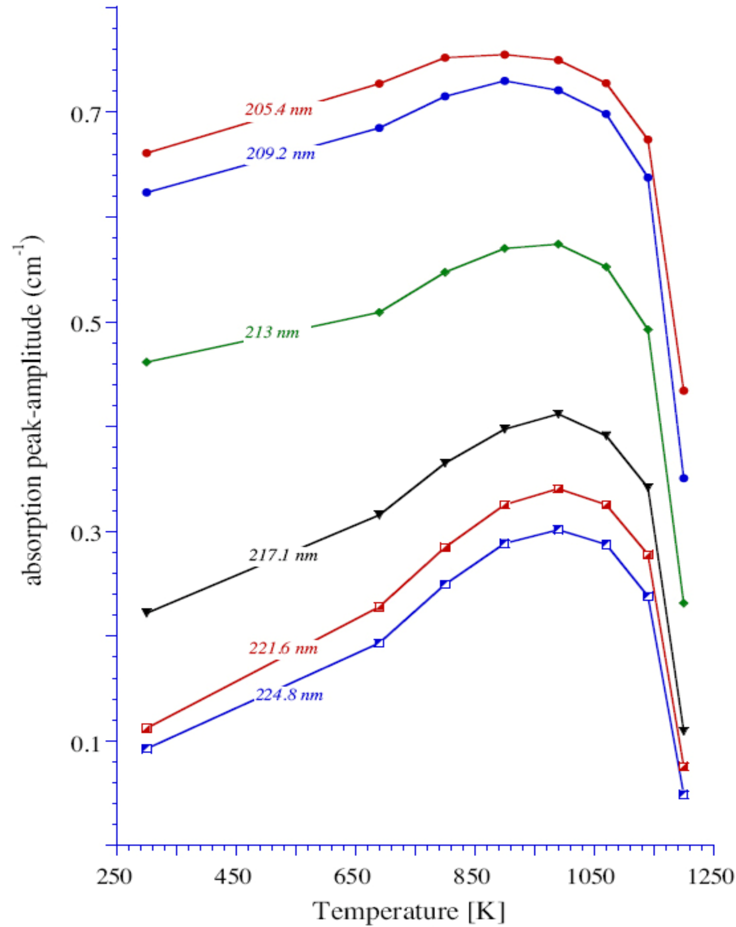

Figure 5. Absorption spectrum of NH_3 decomposition at various wavelengths as a function of temperature.[13]

1.1.4 Substrate requirements to grow high quality GaN

The issues for growing high quality, single crystal GaN are the use of a compatible substrate that has similar lattice and thermal parameters. Conventionally, bulk wurtzite GaN is grown on sapphire (Al_2O_3) primarily due to its hexagonal symmetry and high temperature stability (~1000 ^{o}C)[3]. However, growing GaN on sapphire presents a significant lattice and thermal mismatch which thus gives rise to dislocations at the growth interface between the substrate and the epitaxial layer. A method to alleviate interfacial dislocations is to grow a thin buffer layer of AlN on sapphire, which was done by Amano *et al.*[14] which improved the quality of GaN growth. Dmitriev *et al.*[15] has also grown high quality GaN on 6H-SiC due to its low lattice mismatch and high electrical conductivity. Table 2 shows the difference of both the lattice and thermal parameters between GaN and several substrate materials.

Table 2. Lattice & thermal properties between GaN and its substrates

Substrate	Symmetry	Lattice Parameters [Å]	Coefficient of Thermal Expansion [$\times 10^{-6}$ K^{-1}]
Wurtzite GaN	Hexagonal	$a = 3.189$	5.59
		$c = 5.185$	3.17
Wurtzite AlN	Hexagonal	$a = 3.112$	4.2
		$c = 4.982$	5.3
Al_2O_3	Hexagonal	$a = 4.758$	7.5
		$c = 12.991$	8.5
6H-SiC	Hexagonal	$a = 3.08$	--------
		$c = 15.12$	--------
ZnO	Hexagonal	$a = 3.252$	2.9
		$c = 5.213$	4.75
Si	Cubic	$a = 5.43$	3.59

1.1.5 Functional GaN nanostructures

As discussed earlier, the type of substrate used influences the quality of GaN such that the lattice and thermal mismatches creates defects at the interface and thus leading to device degradation. Although much progress has been made in improving the crystal growth quality of bulk GaN and its application in optoelectronic devices, research on growing GaN in the nanoscale, in particular one-dimensional (1-D) nanostructures (wires, rods, belts, and tubes) has been gaining interest primarily due to its novel physical properties (e.g. quantum confinement, electron transport and magnetic effects). Their physical properties depend on their size and dimensionality [16,17]. They have great potential for applications in photovoltaics, LEDs and various nanodevices[17]. With the dependence of the high surface-to-volume ratio exhibited by 1-D nanostructures, they yield appealing mechanical properties. The advantage of nanowire fabrication over its bulk counterparts is that it gives rise to high quality, single crystal which leads to lower defect density hence attributing to high mechanical strength, stiffness, and toughness nearing theoretical values of ideal crystals.[16] There are two methods in which nanostructures are fabricated that is, the "top-down" and "bottom-up" approaches[18]. The top-down scheme utilizes both nanolithography and etching techniques. Lithography[19] is a patterning technique which involves precise removal of bulk material utilizing soft X-rays or an electron beam operating at the range of several hundred kV to and, etching involves the removal of layers from the substrate, this is done by either ion-beam or wet etching. However, with the precision (namely the minimization of drifting which are caused by charging and distortion at the interferometer) and the high-resolution that is required for nanolithography, high production costs are a consequence[20]. With the bottom-up approach, this is an inexpensive procedure has been an ongoing area of research. The method primarily involves growing one-dimensional nanostructures onto a substrate by the dispersion of atoms and molecules from the vapor for example, the CVD technique which we will discuss mainly.

The important factor of synthesizing high quality, single-crystal nanowires using the bottom-up technique is its growth mechanism. The growth mechanism is an essential concept given that it dictates the desired size, shape, morphology, and the uniformity of

the nanostructure[16]. One-dimensional nanostructures generally are grown along a single crystallographic direction and the various methods that induce this growth consist of growing intrinsically an anisotropic structure, use of templates (such as nanotubes and membranes) and catalysts to guide the formation of the nanostructure, and minimizing the symmetry by employing a solid-liquid interface, etc[16,21]. The synthesis methods used to grow nanowires are the vapor-liquid-solid (VLS) and the vapor-solid (VS) mechanism.

The VLS process was first revealed by Wagner and Ellis[22], who grew silicon whiskers by adding a particle of Au on a surface of a silicon substrate which forms a liquid droplet of Au-Si alloy. The liquid droplet from the metal is a key component to initiating and dictates nanowire growth given that it acts as a catalyst[16,22]. The selection of a suitable metal catalyst to employ the VLS mechanism to successfully grow one-dimensional nanowires is crucial and depends on several factors[22]: (1) how inert the catalyst is to its reaction products, (2) the liquid alloy formation at the deposition temperature, (3) the distribution coefficient and, (4) its vapor-liquid-solid interfacial energies. Figure 6 illustrates the formation of a nanowire using the bottom-up method.

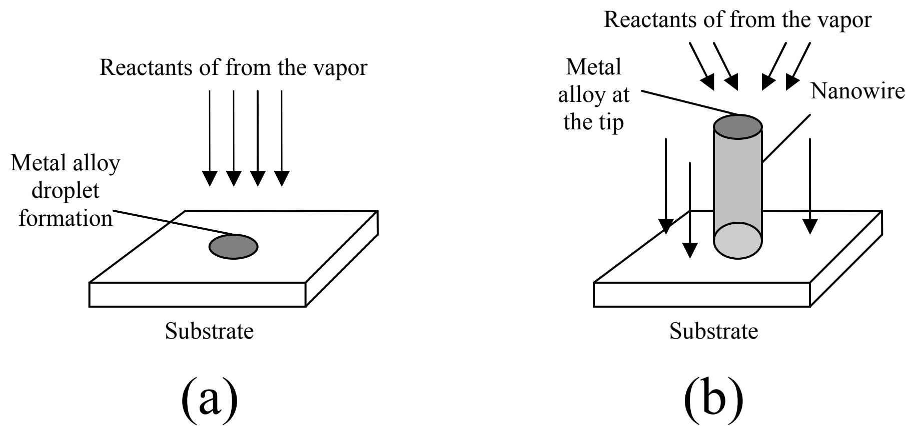

Figure 6. Nanowire growth by the VLS mechanism using the bottom-up approach. A droplet of metal alloy is formed (a) on the substrate from the vapor and acts as a catalyst dictating the axial growth of (b) the nanowire.

As seen in figure 6, the diameter of the nanowire depends[20] on the size of the catalyst droplet. When initiating the VLS mechanism, it is critical that both[8,20] the binary and ternary phase diagrams between the catalyst metal and reactant material are considered that is, for example the formation of Ni-Ga alloy and Ni-Ga-N as NH_3 undergoes stepwise decomposition at the growth temperature when growing GaN nanowires using a Ni catalyst. Figure 7 shows a binary Ni-Ga phase diagram indicating the phases and mixtures present from 300-1200 ^{o}C and figure 8 illustrates an isothermal phase diagram at 500 ^{o}C at 1 bar of pressure. For successful[20] growth of nanowires, the catalyst droplet must have direct contact on the substrate surface with a large adhesion coefficient such that precursor atoms from the vapor disperse on the droplet triggering the alloy formation. Continuous flow and accumulation of atoms from the vapor leads to supersaturation which thus exhibit growth at the solid-liquid interface which the droplet remains at the tip of the nanowire as mentioned in figure 6.

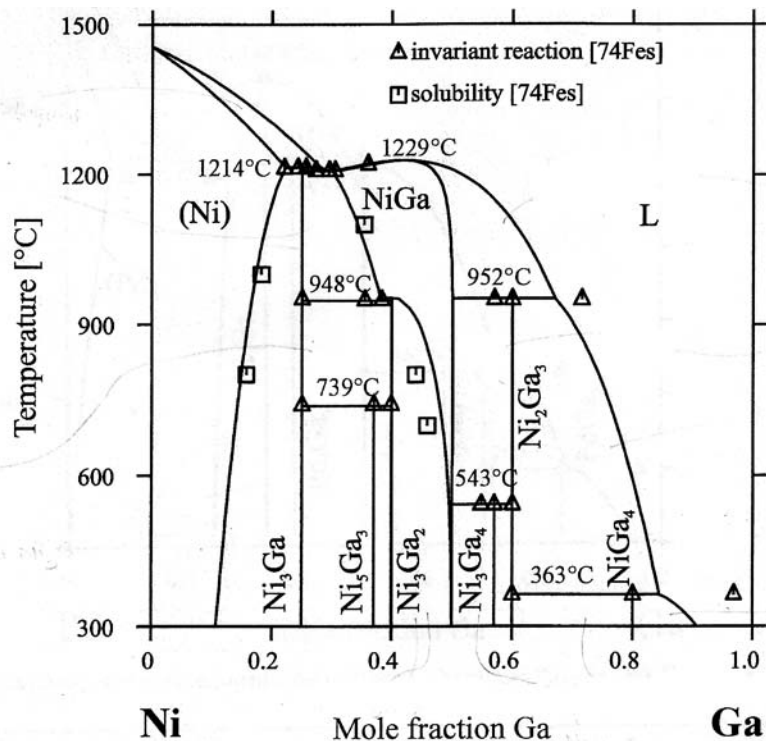

Figure 7. Binary Ni-Ga phase diagram [23] which there are six phases indicating incongruent melting and NiGa being the only solid solution forms congruently. NiGa is stable at 950 ^{o}C with Ga at. % ranging from 35 to 50%.

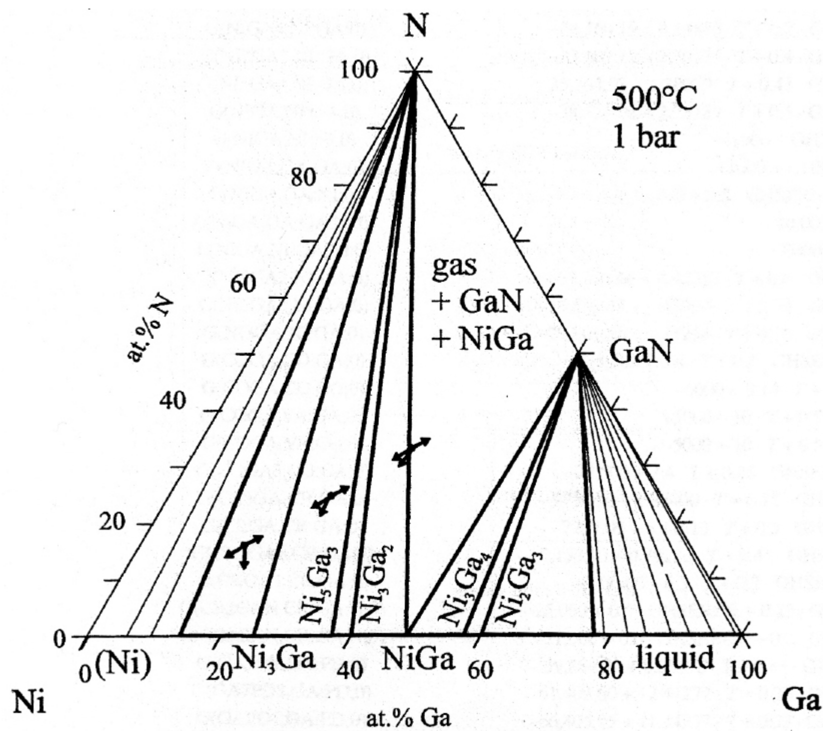

Figure 8. Isothermal ternary [23] Ni-Ga-N phase diagram at 500 ^{o}C at 1 bar of pressure.

The possible disadvantage of utilizing a metal catalyst is the contamination of the grown nanowire and could affect their properties[16]. Self-catalytic VLS growth is possible such that the Ga droplet could play a role as a VLS catalyst[16] as Ga alloys with nitrogen atoms from the vapor and this has been reported when solid Ga has directly reacted with ammonia[24,25,26,27]. Self-catalytic growth has an advantage in which contaminants from elemental catalysts that initiate the VLS mechanism are avoided[16,27]. It is also possible that the self-catalytic VLS growth was revealed by the VS mechanism, in which one-dimensional nanowires was grown without the use of a metal catalyst[16]. The growth of GaN nanowires by the VS process has been reported by He *et al.*[24,25,26]. The thermodynamic and kinetic aspects of this mechanism for the growth of GaN and various III-V binary nanowires have been discussed[27] by S. Mohammed.

He *et al.*[26] have investigated the growth parameters of single crystal GaN nanowires by direct reaction of Ga with ammonia which includes NH_3 flow rate, growth temperature, and chamber pressure. They have obtained different morphologies by varying the NH_3 flow rate while maintaining constant the growth temperature at 900 ^{o}C and chamber pressure at 15 torr. GaN nanowires were obtained at flow rates 40 sccm (standard cubic centimeters per minute), 100 sccm, and 150 sccm; below 40 sccm GaN crystal platelets and, Ga at 20 sccm were observed respectively[26]. When varying the temperature between 825 ^{o}C and 950 ^{o}C while having constant the NH_3 flow rate at 100 sccm and the chamber pressure at 15 torr, the diameter of GaN nanowires increased with increasing temperature. As the chamber pressure was varied along with having the other growth parameters constant, the density and uniformity of GaN nanowire growth was affected and was grown with different morphologies[26].

1.1.5.1 Motivation

Growth of GaN one-dimensional nanostructures using thermal CVD presents a challenge since various factors must be taken into account. The challenges of growing nanostructures are to initiate the alloy droplet, controlling the location of growth at the nucleation sites and, to obtain the desired morphology such as nanowires whereas in bulk growth, thickness control and, having a lattice and thermally compatible substrate is needed in order to grow high quality GaN. As mentioned before, we have to consider the decomposition of NH_3 under catalytic environments, and the type of Ga precursor used. To determine the growth mechanisms involved, we need to understand chemically what is taking place in the reaction zone hence to have better control over the growth under various reaction environments.

In this study, we investigate low temperature CVD growth of 1-D nanostructures. Majority of GaN 1-D nanostructures have been synthesized at high temperatures[26] where GaN has a tendency to decompose (~850 ^{o}C). Low temperature growth of GaN nanostructures could have potential for use of electron emitters[17] and lower the costs of nanostructure fabrication. Chang and Wu[17] have grown GaN nanostructures as low as 550 ^{o}C. The primary motivation in this research area is to employ low temperature CVD growth of GaN nanostructures lower than 550 ^{o}C using various methods under several reaction conditions to obtain not only high yields of GaN but to also attain the desired morphology.

1.2 Experimental Method

GaN nanostructures are grown by the CVD method on a BN (AXO5, Saint Gobain Advanced Ceramics) substrate. Various methods were used to attempt growing nanostructures by:

1. Vaporizing gallium acetylacetonate (Gallium (III) 2,4-Pentanedionate - 99.99%, metals basis, Alfa Aesar Inc.), $Ga(acac)_3$ below its decomposition temperature (~196 ^oC) at a low-temperature region of the single-zone furnace (setup shown schematically[28] in figure 9) and reacting directly with NH_3 gas. For Ni catalyst-induced CVD growth, the catalyst was introduced by spraying the substrates with a 0.01 M ethanol solution of $Ni(NO_3)_2$.

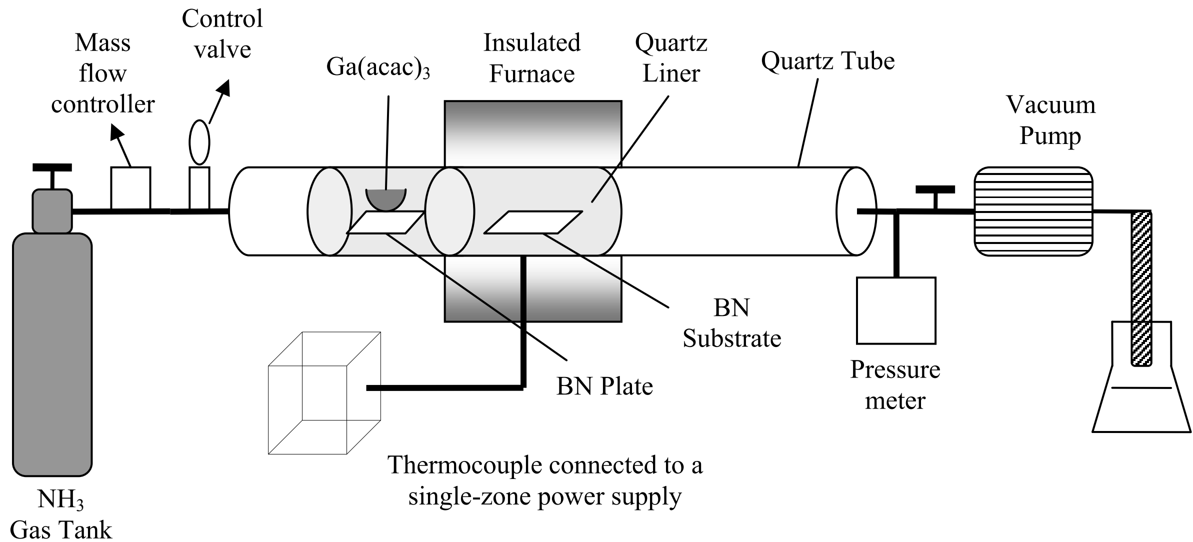

Figure 9. Schematic setup (partially taken from Carvajal et al.[28]) of reacting gallium acetylacetonate, $Ga(acac)_3$ with NH_3.

2. Utilizing ultraviolet beam as a catalytic source to excite NH_3 molecules and using $Ga(acac)_3$ as a gallium precursor, the wavelength was set at 205.4 nm. This was carried out at the U-11 beamline at the National Synchrotron Light Source at Brookhaven National Laboratory. A slight modification in figure 9 is shown schematically in figure 10.

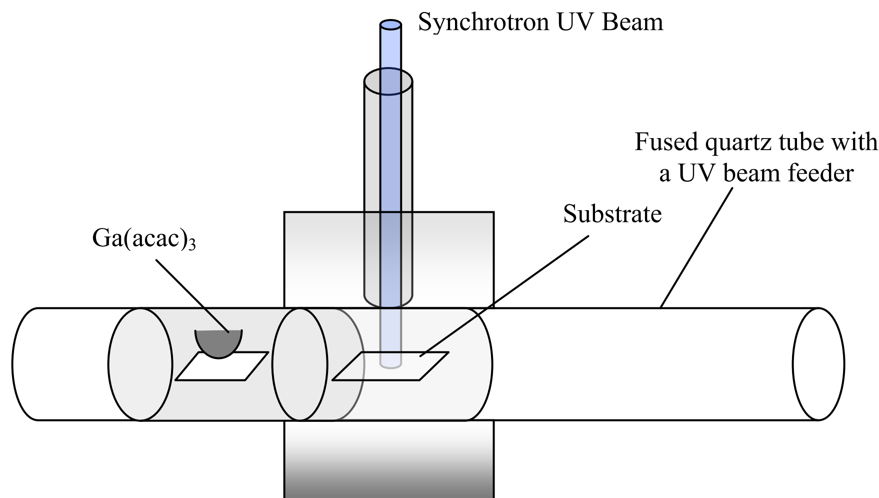

Figure 10. CVD setup using UV-assisted beam

3. Grinding calcium fluoride (CaF_2) into powdered form mixing with a drop of Ga metal. The powder was placed on a BN support with the BN substrate shown in figure 11.

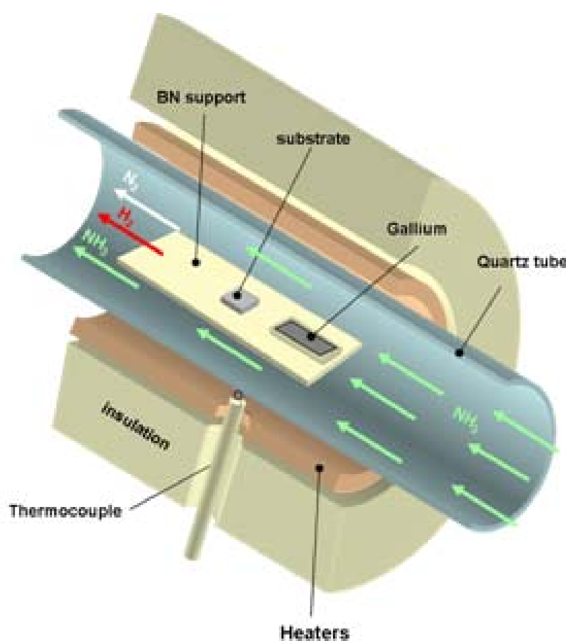

Figure 11. Growth setup using Ga and CaF_2 mixed in powdered form.

Temperature profile measurements shown in figure 12 at several growth temperatures were performed along the length of the quartz tube which we start from the right end point of the insulation. These measurements were performed to determine what temperature corresponding to the position of the quartz tube is suitable to vaporize $Ga(acac)_3$. The temperature distribution was assumed to be symmetric on both left and

right end points of the insulation. A suitable temperature range to vaporize the gallium source was between 150–175°C given that the source may not vaporize sufficiently below and decompose rapidly above this range. Using furnace temperature profile measurements at different set temperatures the appropriate location for the gallium acetylacetonate powder was determined. The powder was held in a quartz container placed on a BN plate placed on the upstream side of the quartz tube at a suitable distance for vaporization.

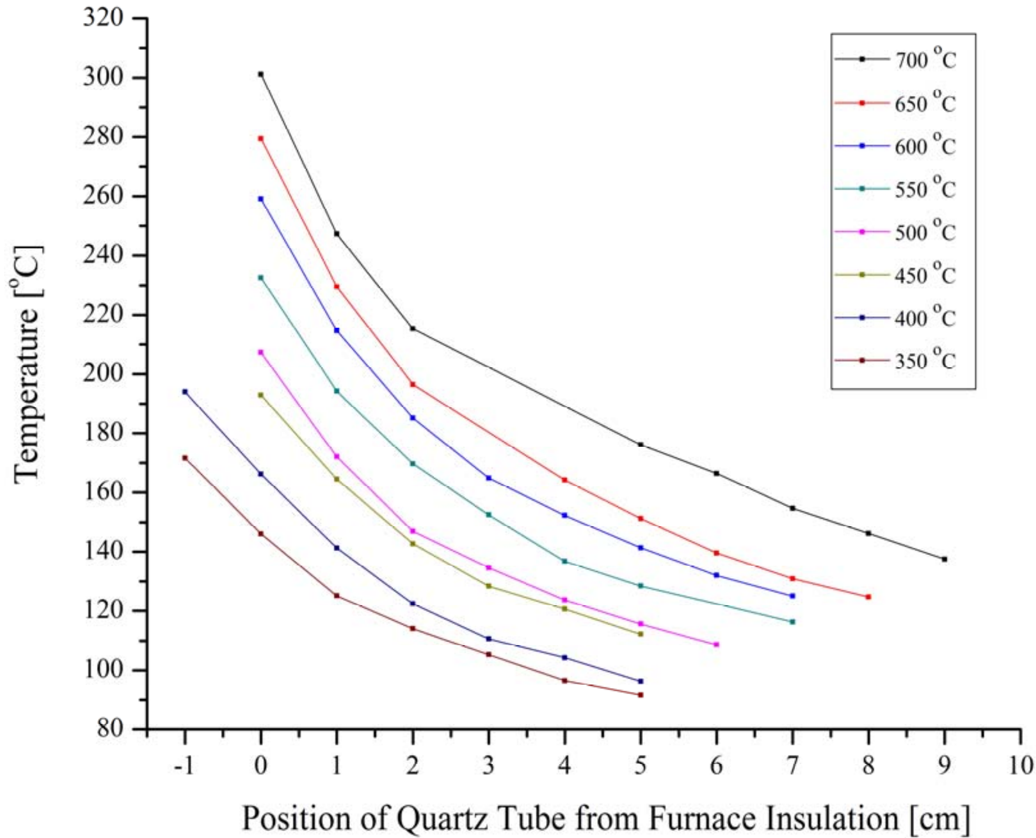

Figure 12. Temperature distribution along the length of the quartz tube at several growth temperatures.

The substrate was placed in the furnace isothermal hot zone. Quartz liners[24] were used to prevent the quartz tube of possible contamination during growth. The furnace quartz tube was first degassed to a vacuum pressure of about 10^{-2} torr and NH_3 was flown at 75 and 100 sccm keeping the pressure constant between 15 to 200 torr depending on the type of growth run. Growth runs were carried out at temperatures ranging from 700 to 400 ^{o}C, starting at temperatures where we can assess that GaN is formed and reducing the temperature until the wurtzite GaN phase is lost. After heating the furnace to the set growth temperature, the reaction zone remained at constant temperature between 1-4 hours and cooled down to room temperature with the NH_3 gas tank turned off. Structural and elemental analyses were carried out by scanning electron microscopy (SEM, LEO

1550 SFEG-SEM) with energy dispersion X-ray spectroscopy (EDX). The crystal structure was analyzed by high-resolution transmission electron microscopy (JEOL JEM 2100F & 3000F HRTEM) at Brookhaven National Laboratory's Center for Functional Nanomaterials. HRTEM samples were prepared by dispersing the nanoparticles on a copper mesh grid covered by a holey carbon film.

1.3 Results & Discussion

1.3.1 GaN growth without the use of a metal catalyst

Growth experiments were carried out without the use of a Ni catalyst to determine whether a yield of GaN is possible. Growth temperatures used ranged from 700 ^{o}C, at which we can assess that wurtzite GaN is formed, down to 450 ^{o}C, until the GaN phase is lost. Sets of experiments were run with 100 sccm NH_3 flow rate with chamber pressure of 200 torr and, 75 sccm flow rate and 15 torr. Growth products obtained on the BN substrates were mostly black and sometimes gray. SEM and EDX studies revealed the formation of GaN of various morphologies down to 450 ^{o}C.

Figure 13 shows an SEM image and an EDX spectrum of the black products grown on the BN substrate at 650 ^{o}C with NH_3 flow rate 100 sccm at total pressure of 200 torr. The SEM image in Fig. 13(a) shows a uniform GaN matrix with a rough surface. The corresponding EDX spectrum (Fig. 13(b)) reveals the presence of both Ga and N and other elements such as O, Si, Cl, K and Ca that are likely contaminants introduced during substrate preparation. The high peak of B in the spectrum indicates that a BN substrate was used while the Au peak is from the gold layer deposited to facilitate conduction.

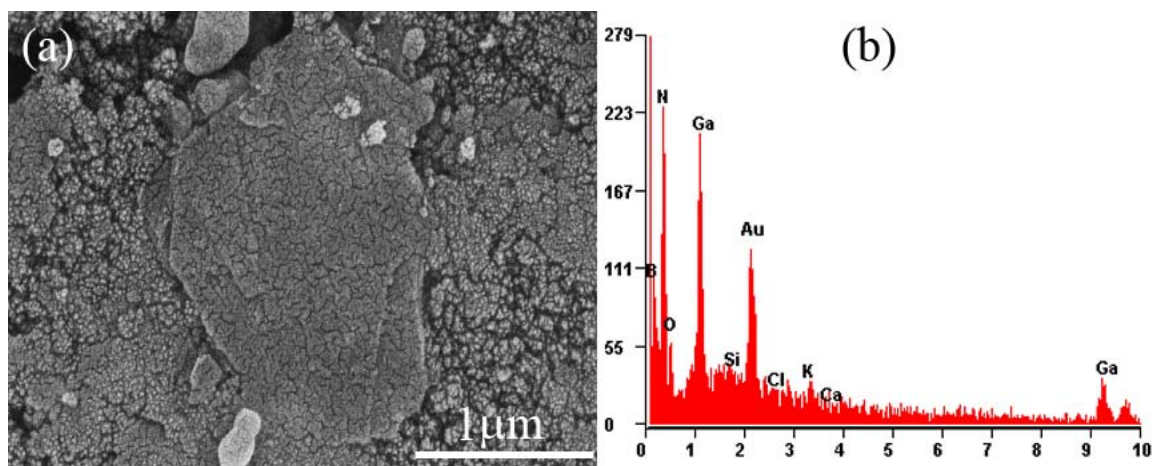

Figure 13. SEM image (a) and the EDX spectrum (b) of the GaN matrix grown at 650 ^{o}C with NH_3 = 100 sccm and p = 200 torr in 160 min.

At 500 ^{o}C at total pressure of 200 torr with 100 sccm NH_3 flow rate, gray colored products were formed. The SEM image in Figure 14(a) shows a clump of GaN nanoparticles and the EDX spectrum (Fig. 14(b)) is similar to the one in Figure 13(b) with a close 1:1 peak correspondence of Ga:N.

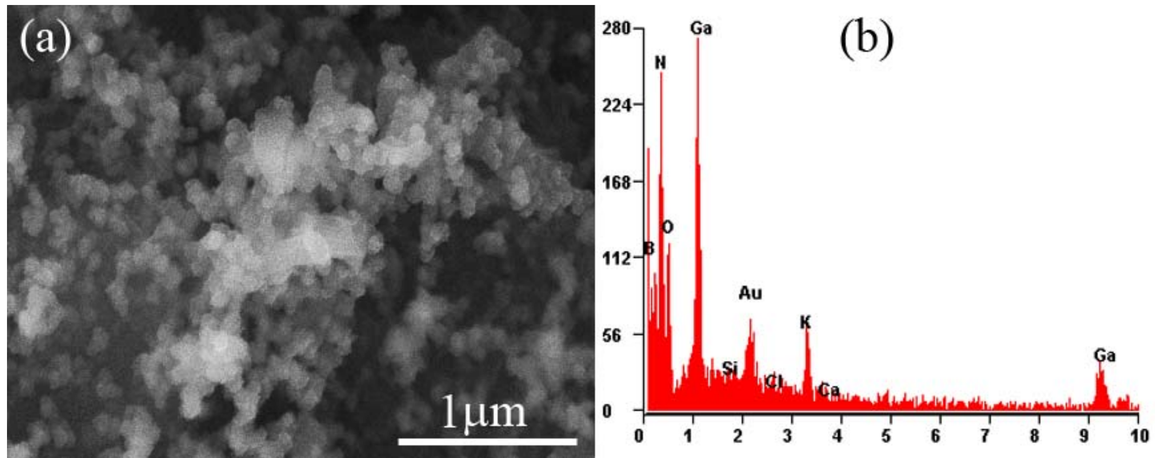

Figure 14. SEM image (a) and EDX spectrum (b) of clumped GaN nanoparticles grown at 500 ^{o}C with NH_3 = 100 sccm and p = 200 torr in 130 min.

However at 450 ^{o}C with the NH_3 flow rate set at 75 sccm and its pressure at 15 torr, a nanoneedle is observed shown in the TEM images in figure 15. The length of the needle extends approximately up to 0.5 μm (figure 15(a)) and its diameter is 58 nm (shown in figure 15(b)). A high resolution TEM image projected along $[1\bar{1}00]$ in figure 15(c) indicates that the lattice spacing is 0.313 nm, which corresponds to the one-half the *d*-spacing of $(11\bar{2}0)$ planes wurtzite hexagonal GaN. Figures 15(d) and (e) shows HRTEM images of regions 1 and 2 respectively as indicated by the broken line box in figure 15(a); it is observed that partial edge dislocations are present along $[11\bar{2}0]$ where an extra half-plane of atoms are introduced shown by the inset.

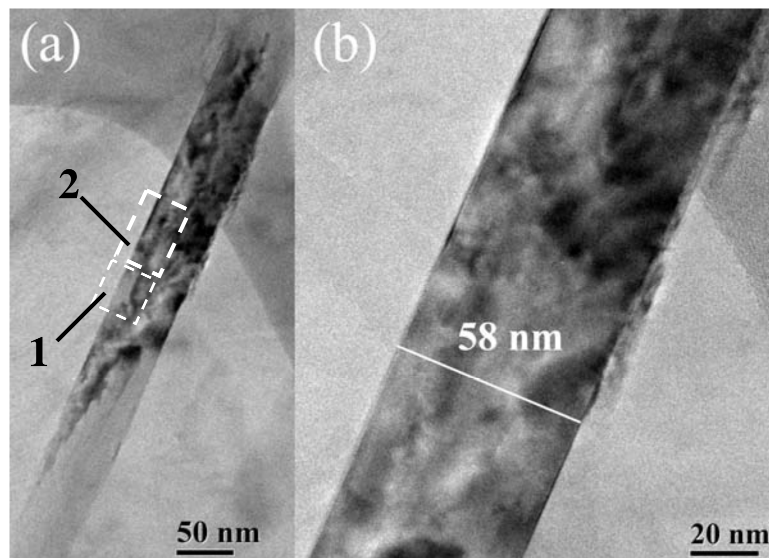

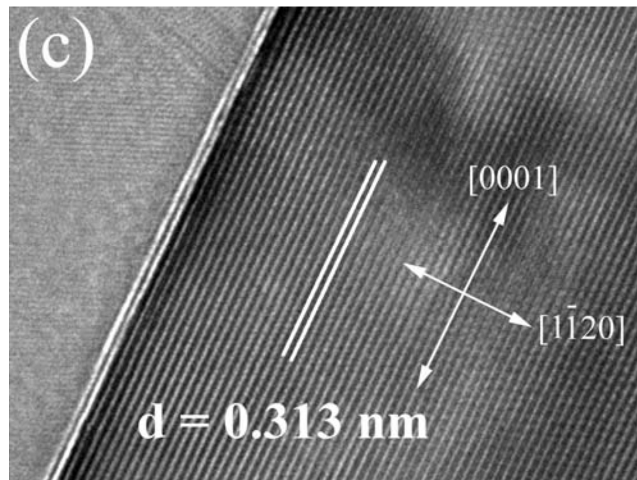
(c)
[0001]
[1$\bar{1}$20]
d = 0.313 nm

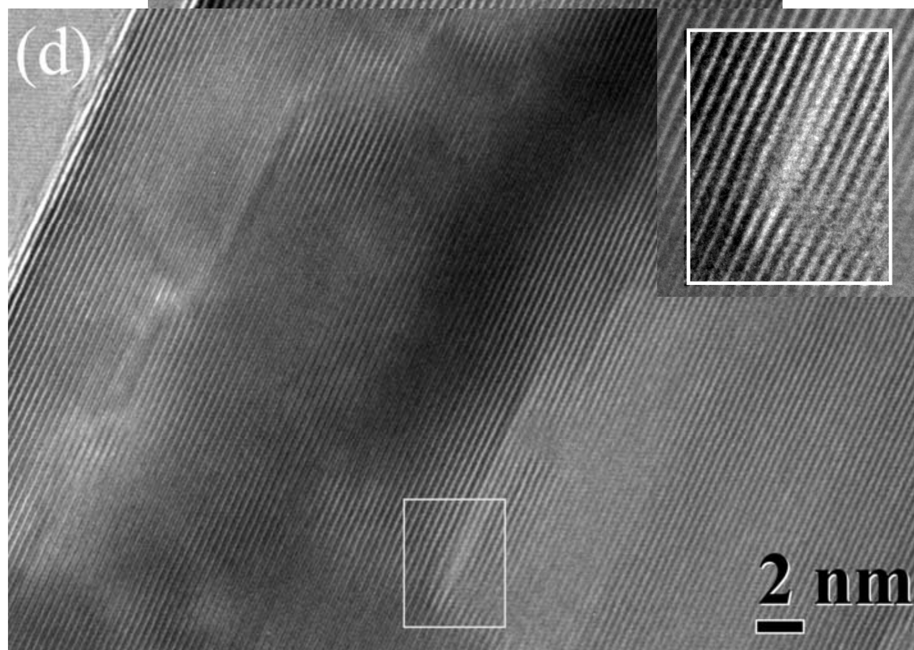
(d)
2 nm

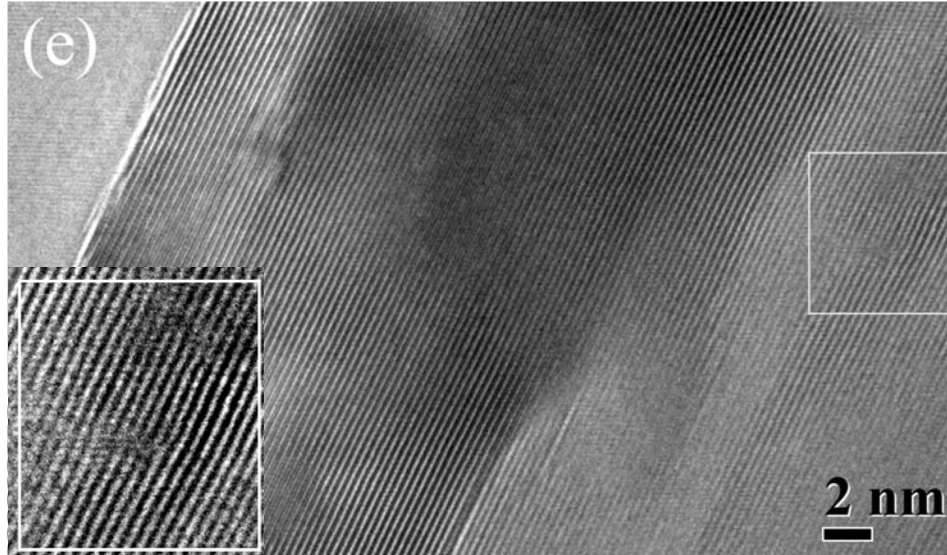

Figure 15. TEM images projected along $[1\bar{1}00]$ of the nanoneedle grown at 450 ^{o}C with NH_3 = 75 sccm and p = 15 torr in 90 mins. (a) TEM image showing the full length of the nanoneedle and, (b) the diameter. (c) HRTEM image showing the lattice spacing. (d)-(e) HRTEM images of regions 1 and 2 indicated by the broken line box in (a) respectively; the inset denotes the partial edge dislocation indicated by the white box.

There are various reactions that can occur when CVD growth is undergoing. One possible reaction is the decomposition of $Ga(acac)_3$ to initiate the formation of Ga atoms from the vapor reacting with NH_3 to form GaN. The Ga atoms act as catalysts for the activation[27] of ammonia undergoing step-wise decomposition to

$$Ga + NH_3 \rightarrow Ga + NH_2 + \frac{1}{2} H_2, \quad [1.5]$$

$$Ga + NH_2 \rightarrow Ga + NH + \frac{1}{2} H_2, \quad [1.6]$$

$$Ga + NH \rightarrow Ga + N + \frac{1}{2} H_2, \quad [1.7]$$

$$Ga + N \rightarrow GaN. \quad [1.8]$$

It is interesting to note that no nanoneedle like morphologies were observed when the NH_3 flow rate and chamber pressure were set at 100 sccm and 200 torr respectively. However, Mohammed has reported[29] that the nanowire density increases with both increasing NH_3 flow rate and chamber pressure at a fixed temperature. This is not the case although GaN was obtained in the form of nanopowders, this is probably due to the lack of adsorption of NH_3 molecules at the nucleation sites most which is most likely caused by the turbulent gas flow[27,29] in the system. Thus setting the flow rate to 75 sccm and 15 torr pressure probably had slight lower turbulent flow which possibly induced the growth of the nanoneedle. The formation of the liquid droplet to initiate the self-catalyzed VLS mechanism was not observed and conditions applied here are probably not favorable

for rapid GaN synthesis through the initiation of some type of vapor-solid nucleation mechanism.

1.3.2 GaN growth with the use of a metal catalyst

Based on prior studies on the use of a catalyst to initiate vapor-liquid-solid (VLS) growth[16], we have used Ni catalyst directly on the BN substrates and attempted to growth GaN nanopowders from 500 to 400 ^{o}C. At 500 ^{o}C at total pressure of 200 torr a gray substance was formed on the substrate. The SEM image in Figure 16(a) illustrates scattered and clumped nanoparticles of GaN grown on the substrate indicated by white spots and has a similar morphology to the micrograph in Figure 14(a). The EDX spectrum in Figure 16(b) shows a high 1:1 peak ratio of Ga:N. The high peak of Au is attributed to the long period of treatment on the substrate as a conductive layer used for SEM analysis. The Ni present in the spectra corresponds to the catalyst used on the BN substrate.

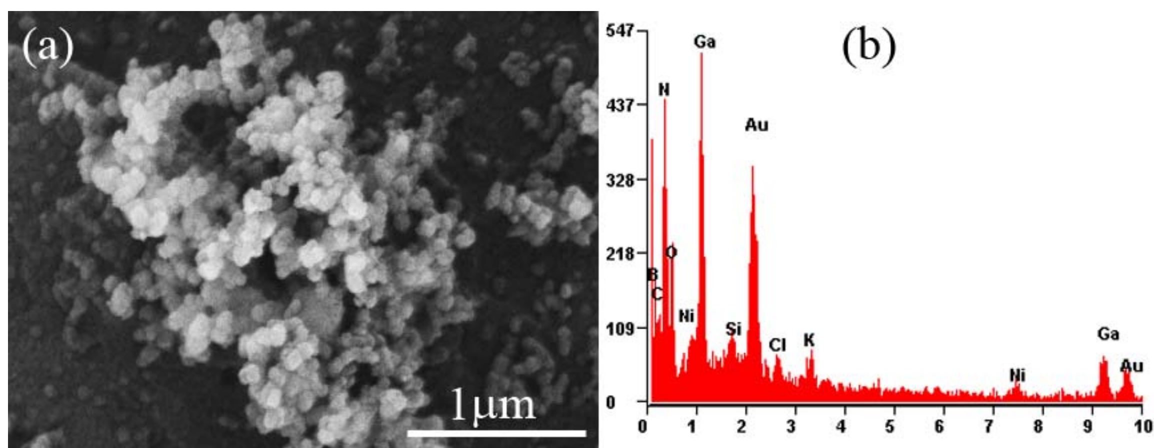

Figure 16. SEM image (a) and EDX spectrum (b) of clumped GaN nanoparticles grown via Ni catalyst at 500 ^{o}C (NH_3 = 100 sccm, p = 200 torr) in 130 min. The nanoparticle size estimates from 75 ~ 90 nm.

Similar results are also obtained at 450 ^{o}C at total pressure of 35 torr as shown in figure 17. Selected area diffraction pattern (SAED) analyzed by HRTEM with its incident beam oriented perpendicular to the basal plane reveals that the crystal structure is wurtzite GaN single crystal.

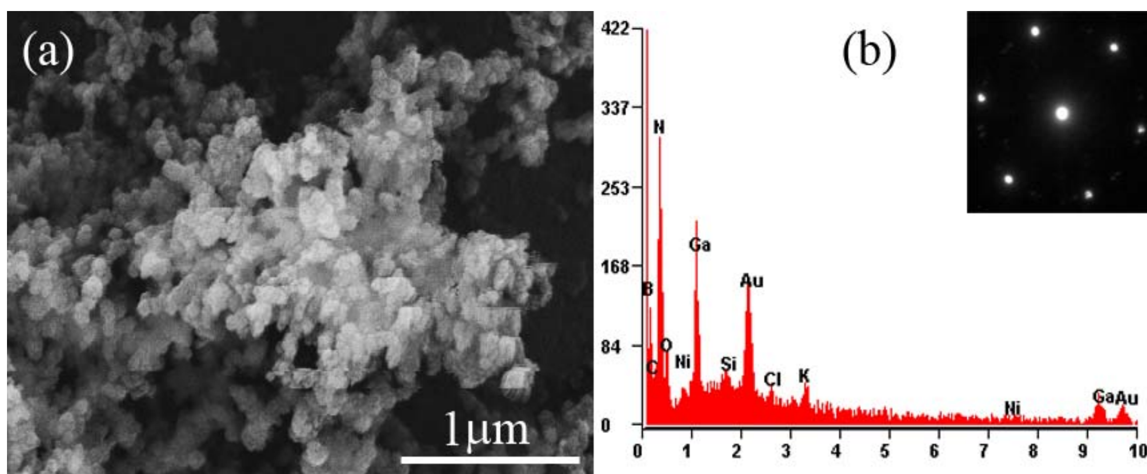

Figure 17. SEM image (a) and EDX spectrum with the corresponding SAED pattern inset (b) of clumped GaN nanoparticles grown via Ni catalyst at 450 ^oC (NH_3 = 100 sccm, p = 35 torr) in 120 min. The nanoparticle size ranges from 100 ~ 130 nm.

At 400 ^oC at total pressure of 20 torr, dark brown and yellow products were formed on the BN substrate. SEM analysis (Fig. 18(a)) reveals a 0.5 to 1 μm sized porous-like polycrystalline platelets. EDX (Fig. 18(b)) reveals that the porous platelets have a high concentration of Ga. The TEM image (Fig. 18(c)) shows platelets with diameters ranging from 110 ~ 140 nm. The lattice parameters measured from these SAED patterns reveal that the structure of such porous platelets is wurtzite type GaN single crystal, and could be clearly distinguished from the patterns obtained for the BN substrate.

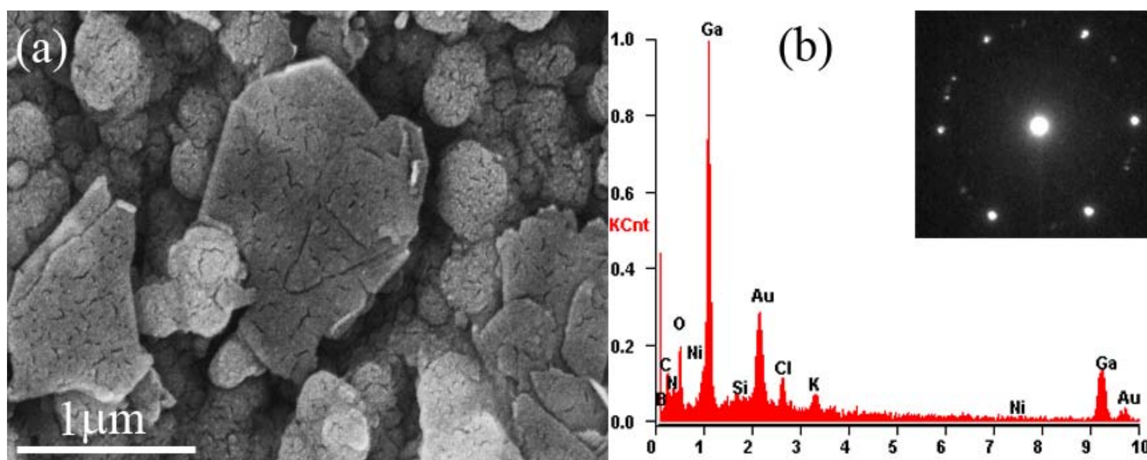

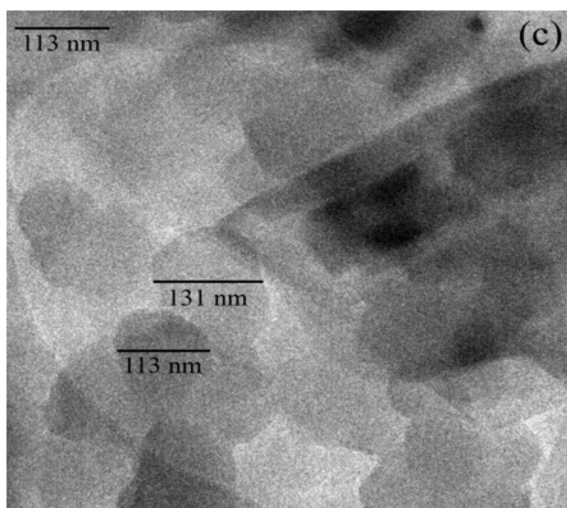

Figure 18. SEM image (a) EDX spectrum with the corresponding SAED pattern inset (b) and (c) TEM image of GaN porous platelets grown via Ni catalyst at 400 ^oC (NH_3 = 100 torr, p = 20 torr) in 240 min.

The use of a metal catalyst has clearly resulted in a yield of GaN nanopowders due to the thermal decomposition[11] of NH_3 at low temperatures. The morphologies obtained are similar to results previously discussed with NH_3 flow rate set at 100 sccm and chamber pressure of 200 torr. This is again likely due to the lack adsorption of ammonia molecules on the BN surface from the turbulent gas flow[27,29]. The use of polycrystalline BN in place of Si as substrate[30] probably resulted in an inhomogeneous dispersion of Ni catalyst and consequently leads to formation of clumps of GaN at locations where the Ni nanoparticles are concentrated. The vapor-liquid-solid (VLS) mechanism[16] is likely operative here and is clearly favorable for GaN synthesis from an organometallic Ga source. However, growth without the use of a metal catalyst would be preferable to avoid contamination. It is remarkable that GaN nanopowders have been produced at a much lower temperature on BN substrates than on Si substrates[30]. This may be attributed to the fact that BN has a hexagonal structure, much closer to the wurtzite structure of GaN than Si, which has a cubic structure. This would facilitate the formation of wurtzite GaN nanopowders on BN substrates.

1.3.3 UV-assisted GaN growth

Experiments were carried out without the use of a foreign metal catalyst here. We report growth of GaN with nanoneedle like morphology from 600 to 450 ^oC on BN substrates with the assist of UV beam to excite and decompose the NH_3 molecules into nitrogen atoms with a wavelength of 205.4 nm. The reason of choosing the wavelength of 205.4 nm is that the absorption peak amplitude is highest at this value compared to other wavelengths as indicated previously in figure 5. Gray products were formed on the substrates. The NH_3 flow rate and chamber pressure was set at 75 sccm and 15 torr respectively with a reaction time of 90 minutes.

At 600 ^oC, the SEM micrograph shows nanoneedles with lengths extending from 1-3 μm were self-nucleated on several facets on the BN substrate due to its

polycrystalline nature as shown in figure 19(a). A high resolution TEM image in figure 19(b) projected along $[1\bar{1}00]$ shows the interplanar lattice spacing of 0.312 nm, which is half the lattice spacing of the $(11\bar{2}0)$ crystal planes of wurtzite GaN. The diameters of the nanoneedles were measured by TEM and are shown in figure 19(c) and 19(d) which illustrates one of the nanoneedles having a diameter of 11.5 and 13 nm respectively.

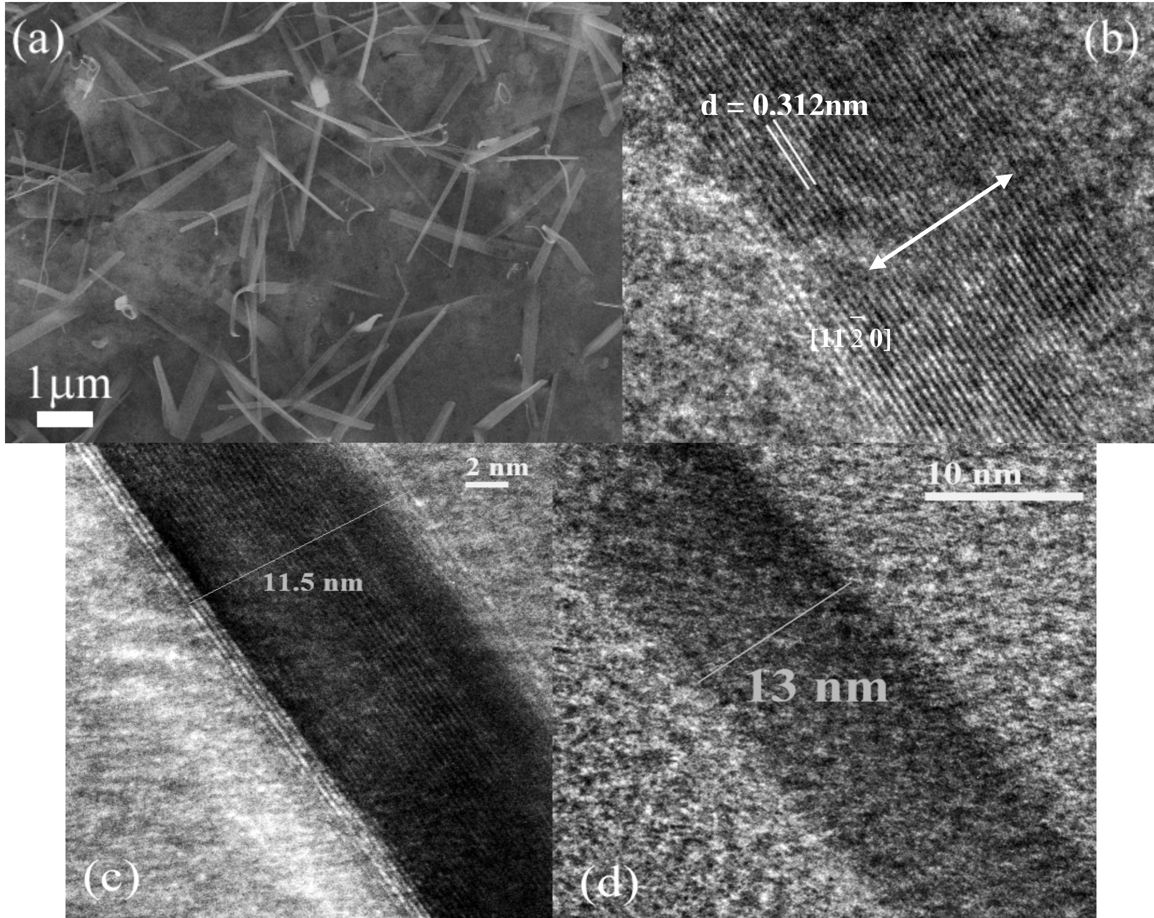

Figure 19. SEM image (a) and, HRTEM images projected along $[1\bar{1}00]$ (b) showing the lattice spacing and (c)-(d) of GaN nanoneedles grown at 600 ^{o}C illustrating the diameters of the nanoneedles and confirming its crystal structure.

At 450 ^{o}C, the lengths of nanoneedles with a stem-like morphology extend from 1-2 µm as they are nucleated along various facets illustrated by the SEM micrograph in figure 20(a). The HRTEM in figure has a lattice spacing of 0.320 nm, which has a similar interplanar spacing as previously indicated in figure 19(b) at 600°C, having half the atomic spacing of the $(11\bar{2}0)$ planes of wurtzite GaN. The low-magnification TEM image in figure 20(c) shows one of the nanoneedles having a diameter of 32 nm.

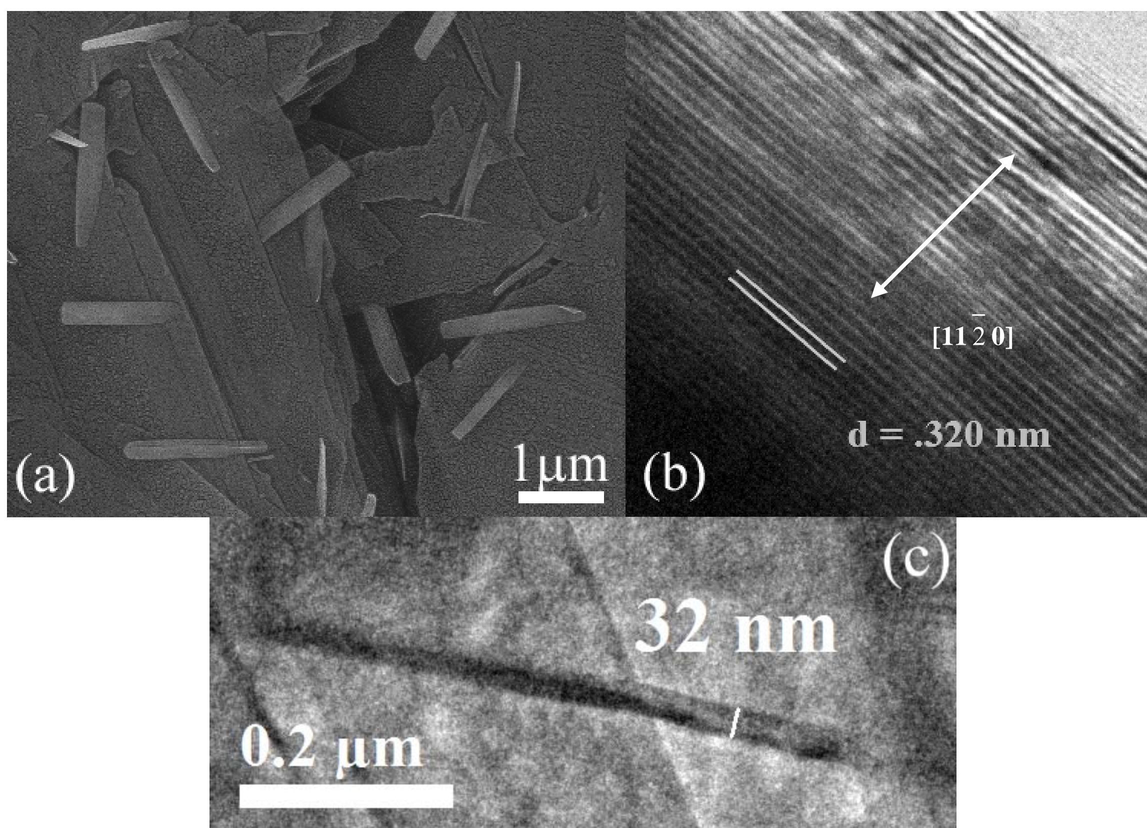

Figure 20. (a) SEM image of stem-like nanoneedles grown at 450 ^oC. (b) HRTEM showing the interplanar spacing and (c) low-magnification TEM indicating the diameter of the nanoneedle of 32 nm.

There is a high density of nanoneedles when using the UV beam. With the difficulty of thermally decomposing NH_3 without the use of Ni catalyst, UV-assisted growth would be the preferred method to employ low temperature growth because of its high absorption[13] of ammonia.

1.3.4 Growth using powdered mixture of Ga and CaF_2

A drop of liquid Ga metal mixed with bulk CaF_2 crushed in fine powdered form was used to attempt growing nanostructures. This method was used primarily to increase the surface area of Ga particles and to increase the rate of reaction. At 650 ^oC, the SEM micrograph in figure 21(a) shows a large CaF_2 particle extending over 50 μm. We would expect that there would be GaN nanorods nucleating from the CaF_2 particle illustrated by the white spots (magnified in figure 21(b)). However the EDX spectrum in figure 21(c) shows otherwise indicating the rods are not GaN, they are CaF_2 crystallites indicated by the high signal of Ca.

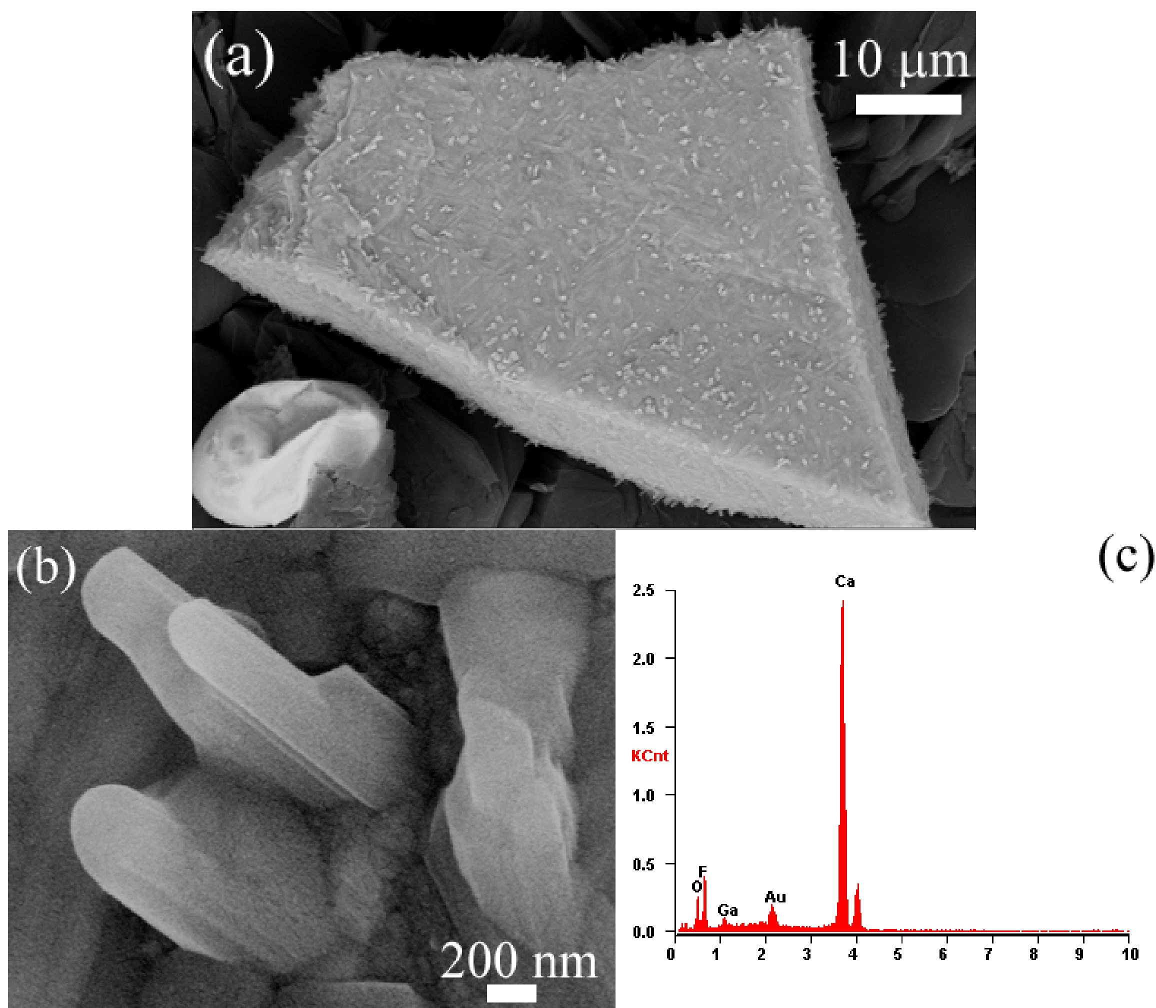

Figure 21. (a) SEM micrograph of the CaF_2 particle. (b) SEM image of (a) under high magnification illustrating the CaF_2 crystallites. (c) EDX spectrum of (b).

The temperature was not sufficiently high to initiate the alloy droplet to form a solid-liquid interface required for growing nanostructures hence there was no GaN present. As discussed previously[20], the droplet must have direct contact on the substrate surface with a large adhesion coefficient such that precursor atoms from the vapor disperse on the droplet triggering the alloy formation.

1.4 Conclusion

In summary, we have synthesized GaN nanopowders through reaction between gallium (Ga) atoms from the decomposition of gallium acetylacetonate and ammonia (NH_3) gas molecules at temperatures as low as 500 ^oC without a catalyst and as low as 400 ^oC using a Ni catalyst. These are the lowest temperatures reported for GaN synthesis so far. Nanoneedles were observed as low as 450 ^oC with a 75 sccm NH_3 flow rate and chamber pressure of 15 torr whereas nanopowders was evident with 100 sccm flow rate with pressures ranging from 20 to 200 torr. The type of fluid flow (e.g. turbulent or laminar) that is undergoing in the reaction zone could likely influence the type of

morphology obtained on the BN substrate. The ammonia molecules do not adsorb readily on the surface as a result and the growth of nanoneedles is preferred when the flow is laminar[27]. The nanoneedles that were grown non-catalytically were observed to have partial edge dislocations. High densities of nanoneedles were observed when using UV radiation, the diameters ranged from 10 ~ 30 nm whereas non-catalytically, the diameter was 58 nm. It is also possible that the self-catalyzed VLS mechanism is not taking place since the alloy droplet of the nanoneedles grown from the BN facet was not observed. The method of using powdered Ga mixed with CaF_2 resulted in no yield of GaN in which the temperature was not sufficient to initiate the liquid alloy droplet required to grow nanostructures.

2. Stress Analysis of Multicrystalline Silicon for Solar Cells

2.1 Introduction

Majority of solar cells that are commercially produced come from silicon. Conventionally, solar cells operate with on single junction namely the *p-n* junction shown in figure 22. In a *p-n* junction solar cell, photons enter the conductive layer and are converted to charge carriers (electrons and holes) which are collected at the contacts. The drift of carriers is driven by an electric field at the junction acting as a circuit and, the depletion layer plays a role in counteracting poor diffusion[31].

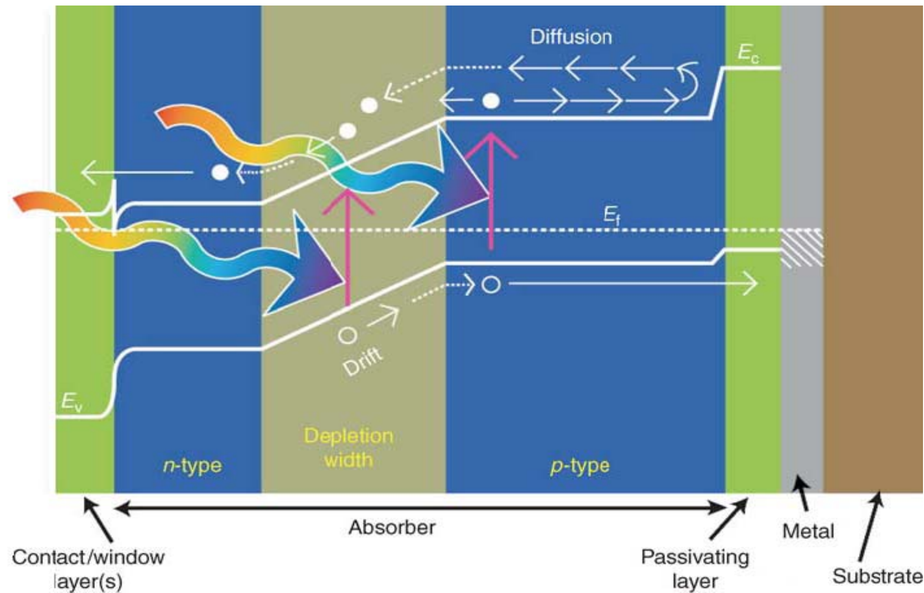

Figure 22. Representation of a *p-n* junction solar cell illustrating the carrier generation from the interaction of photons, E_v is the valence band energy, E_f is the Fermi energy and E_c is the conduction band energy.[31]

Although most solar cells are manufactured using single crystal silicon (sc-Si) which has high solar conversion efficiency, the progress of improving the solar efficiency using multicrystalline silicon (mc-Si) has been an ongoing development due to the significant cost reduction of producing mc-Si. The efficiencies[31] for both sc-Si and mc-Si are 24.7 and 20.3% respectively.

The limitation of mc-Si solar cells is its minority carrier recombination, which are dependent on the density of dislocations attributed by thermal stresses during crystal growth[32]. Most of the production involves the wafer slicing of band sawed columns of as-grown silicon ingots by multi-wire slicing with the consequence of high fabrication costs which are mainly caused by wafer breakages resulting in the loss of silicon (~50 %) hence reducing the production yield[32].

2.1.1 Crystal growth techniques for mc-Si

Mc-Si is grown by an ingot or sheet technique[32]. Figure 23 illustrates schematically the crystal growth techniques.

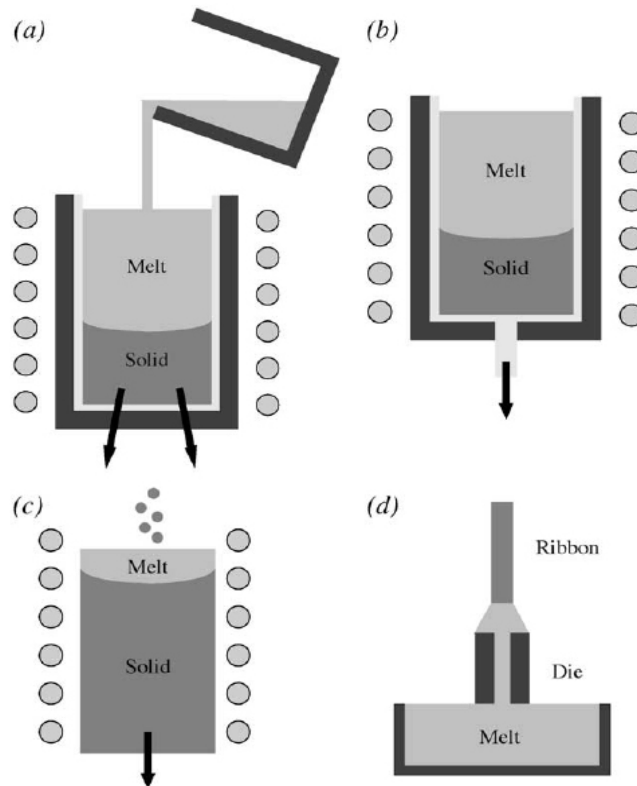

Figure 23. Schematic representation of both ingot and sheet techniques.[32] (a) Bridgman technique, (b) Heat extraction method (HEM), (c) Electromagnetic casting (EMC) technique, (d) Edge-defined-film-fed-growth (EFG) sheet technique.

The Bridgman technique consists of having molten silicon transferred in a crystallization crucible and is solidified over time. Impurities are present along the walls of the crucible, normally containing SiO_2, Si_3N_4 and graphite which thus are collected on the melt. The heat extraction method (HEM) is a modified Bridgman technique where heat is extracted at the bottom of the crucible to maintain a uniform grain structure. The electromagnetic casting (EMC) technique involves having the maintaining the melt by electromagnetic forces and without the use of a crucible but at a consequence of higher stresses and lastly, the sheet technique (e.g. edge-defined-film-fed-growth) requires pulling a ribbon of Si from the melt. Taking into account into the final crystal quality, none of these growth techniques mentioned have a clear advantage.

2.1.2 Wafer processing – Solar cell fabrication

Silicon wafers are processed in various stages[33] to finalize the fabrication of a solar cell. Wafers are first chemically etched in either NaOH or KOH solution to remove highly distorted layers. They are then processed in a cleaning stage where contaminants such as K^+ (or Na^+) ions from etching and impurities are removed by immersing into

various solutions (deionized H_2O, H_2SO_4, and HF) before *n*-type doping (on *p*-type Si) takes place. After doping, a dielectric of SiO_2 is deposited[34,35] on the *n*-type layer as a selective mask to control the diffusion depth and prevents high temperature diffusion of donor and acceptor impurities through Si. An antireflective coating (ARC)[33] usually titanium oxide, having superior optical properties[36] due to its high refractive index is deposited to minimize the energy loss due to reflection before screen printing of both front and back aluminum (Al) contacts, thus obtaining the finalized product of a solar cell shown schematically in figure 24.

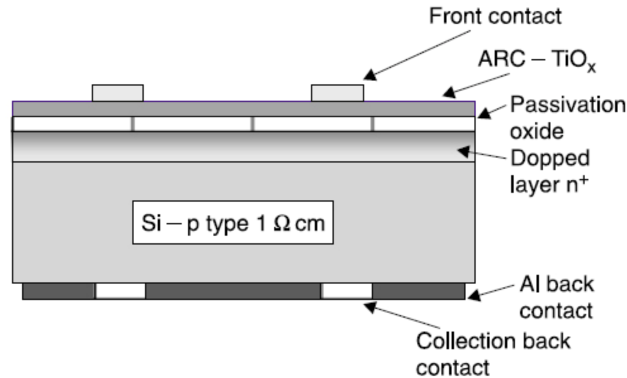

Figure 24. Schematic representation of a solar cell with titanium oxide (TiO_x) as an ARC and, printing of front and back Al contacts.[33]

2.2 Motivation

As previously discussed, stresses generated during crystal growth of ingots and subsequent processing into wafers can lower yield significantly leading to substantial loss of silicon. Studying the stress distribution on the surfaces of as-cut bricks band-sawn from silicon ingots and, the microstructure within the sliced wafers processed through various stages is thus critical to efficient production of solar cells. The primary motivation is to gain a detailed understanding of the stress generation and distribution at each stage of the manufacturing process to improve processing strategies to reduce the thermal stresses during crystal growth and to increase yield of solar cell panels.

2.3 Experimental

The bricks band-sawed from mc-Si ingots and wafers wire-sliced from the bricks were provided by BP Solar Inc. The procedure characterizing its grain structure, strain level and dislocation content of mc-Si at each stage of the processing sequence was carried out by using the technique of synchrotron white beam X-ray topography (SWBXT) in various recording geometries depending on the type of sample (i.e. ingot/wafer). SWBXT has been carried out at the Stony Brook Synchrotron Topography Facility, Beamline X-19C at the National Synchrotron Light Source at Brookhaven National Laboratory. For brick samples, X-ray topography was carried out in the reflection geometry and the different grains on each face were imaged using several X-ray films with a sample-to-film distance of 35 cm. X-ray images of the different grains in the boule were then reconstructed using image processing software to obtain an overall picture of the boule quality. In case of the reflection geometry, the surface is sampled

upto a depth of about 10 microns. Wafers sliced from the bricks were thin enough to allow the use of transmission geometry with a 20 cm sample-to-film distance. Several images were recorded and the entire wafer reconstructed for evaluation of wafer quality. In case of transmission geometry, the information is averaged over the entire thickness. Schematics of the recording geometries for both the brick and wafer are shown in figure 25.

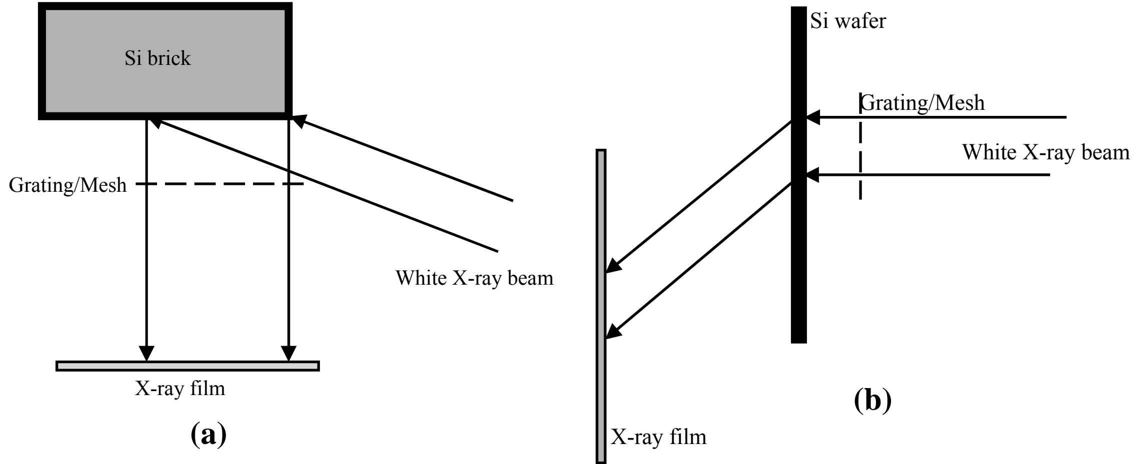

Figure 25. Recording geometries for synchrotron white beam X-ray topography / reticulography (a) Reflection geometry employed for recording topographs and reticulographs from surface of mc-Si brick; (b) Transmission geometry employed for wafers recording topographs and reticulographs from wafers (Note: Grating is employed only during recording of reticulographs).

2.3.1 Synchrotron X-ray Topography

The non-destructive technique of X-ray diffraction topography is used to image defects in bulk, single crystal materials which provides information on the microstructure such as the effect of grain boundaries, and dislocations (if also subjected to mechanical and, thermal stresses from nucleation) [37] . Synchrotron radiation has advantages of providing high intensity, excellent collimation and low beam divergence angle ($\sim 2 \times 10^{-4}$ rad), long source-specimen distances leading to very high spatial resolution and allows maximizing the beam size to image the sample. Defects are revealed if the spatial resolution is adequate. The resolution R depends on its source dimension S perpendicular to the incidence plane, specimen-film distance D and, the source-specimen distance C given by

$$R = \frac{SD}{C} \qquad [2.1]$$

The theoretical resolution at beamline X-19C at the National Synchrotron Light Source is ~0.04 µm/cm of specimen-film distance[37]. The energy ranges from 6 keV (~ 2.1 Å) to 41 keV (~0.3 Å).

Topography can be employed in either transmission or reflection geometries. Transmission geometry is used for samples with low absorption and thickness of a few hundred microns. Reflection geometry is employed for thick crystals and is required when high absorption conditions or high defect densities preclude the use of transmission geometry.

X-ray topography is based on the Bragg law

$$\lambda = 2d\sin\theta_B \qquad [2.2]$$

where θ_B is the Bragg angle and d is the spacing between diffracting planes and produces a diffracted spot. Each diffracted spot is a X-ray topograph where information is present in the form of contrast that arises from variation in diffracted intensity. The diffracted intensity is both a sensitive function[37] of lattice distortion and, absorption conditions in the crystal depending on the type of distortion present. Two fundamental contrast mechanisms are evident in X-ray topographs[37]: (1) orientation contrast and (2) extinction contrast. Extinction contrast can further be classified into three types: (a) direct image (b) dynamical and, (c) intermediary contrast.

Orientation contrast arises from overlap or separation of diffracted X-rays with varying directions caused by inhomogeneous intensity distributions. This is observed in crystals consisting regions of different orientations specifically grains, subgrains, and twins. Occurrence of orientation contrast depends on both the nature of X-rays (i.e. monochromatic or white beam) and the misorientation as illustrated in figure 26. For the case of figure 26(a), if the incident beam divergence or the range of wavelengths available in the incident X-ray spectrum is smaller than the misorientation between the blocks projected onto the incidence plane, then one set of blocks can diffract at a given moment[37]. The presence or absence of diffracted intensity will be produced as a result hence the Bragg condition will be satisfied only at regions where the Bragg angle corresponds to the set wavelength. However, if each block diffracts independently for the case of both monochromatic (shown in figure 26(b) where it is valid when the beam divergence is greater than its misorientation between blocks) and white beam (in figure 26(c)) X-rays, then the diffracted beams emitted from the individual blocks will travel in slightly different directions resulting in image overlap if they converge, or separate if they diverge.

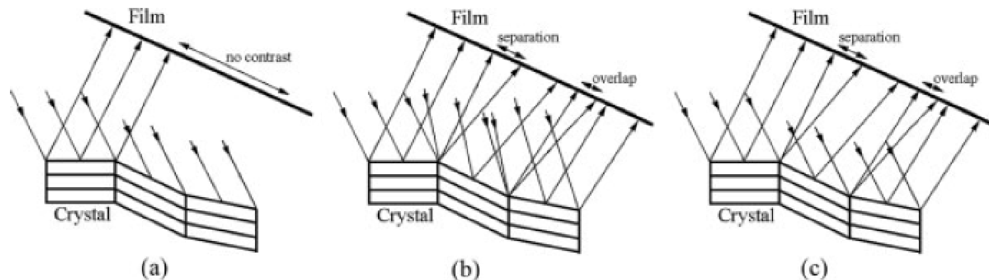

Figure 26. Orientation contast arising from misoriented regions[37]: (a) monochromatic radiation (beam divergence < misorientation); (b) monochromatic radiation (beam divergence > misorientation); and (c) continuous radiation (e.g. synchrotron white beam)

Extinction contrast (which is a dynamical diffraction effect) takes place when the scattering power around defects differs from that of the whole crystal. The three different types of extinction contrast as stated earlier consist of direct, dynamic, and intermediary contrasts which are evident in dislocations and various defects. The types of contrast is determined by the absorption conditions[37], which is defined by the product of the linear absorption coefficient μ and the crystal thickness t namely μt. When topographs are recorded under low absorption conditions ($\mu t > 1$), the dislocation image is dominated by direct contrast. Under intermediate absorption conditions ($5 > \mu t > 1$), all three types of contrast can contribute and for high absorption ($\mu t > 6$), dynamical contrast is dominant. More details on the extinction contrast formation mechanisms can be found in literature 37, 38.

2.3.2 Synchrotron X-ray Reticulography

By utilizing SWBXT to characterize qualitatively its strain levels, a slight modification to SWBXT was used to obtain quantitative information across the surface of bricks and wafers (as seen previously in figure 25), namely the technique of X-ray reticulography. In this technique[39], an X-ray absorbing mesh/grating is placed between diffracting specimen and the detector (X-ray film) or, in the path of the incident beam (see figure 27). The mesh splits the diffracted beam into an array of microbeams. Orientation differences between the crystal elements reflecting individual microbeams are measured by tracking the angular dispersal of microbeams as the mesh-to-plate distance, *M*, is changed. A reticulograph then gives directly a true map of misorientation vectors over the area of the specimen imaged. This method is suitable for mapping and quantifying long range deformation that do not result in the formation of dislocations or grain boundaries.

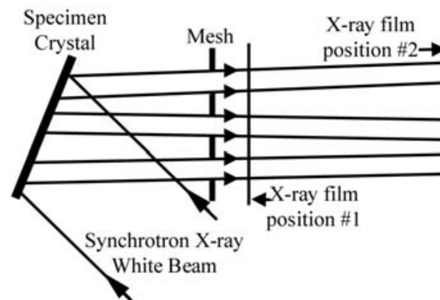

Figure 27. Schematic for synchrotron white beam X-ray reticulography (SWBXR) measurements.

By employing this modification, a coarse mesh with approximately 1mm spacing was used. The distortion of the grating due to strains is then mapped across the entire surface of both the brick and wafer.

2.3.3 Principle of strain/stress measurements using SWBXT

As shown in figure 28(a), the application of shear strain tilts the diffracting plane. The tilted plane will automatically select the wavelength in the white beam which satisfies the Bragg rule and produces a diffracted spot which is shifted from the original

unstrained location by ΔS (see figure 28(b)). The magnitude of the orientation contrast shift is $\Delta S = 2\alpha L$, where α is the maximum apparent shift in the Bragg angle due to the strain induced tilt of the diffracting planes and L is the sample-to-film distance. Assuming that this tilt is induced only by shear strain, we can estimate the magnitude of strain in the underlying silicon die via the equation,

$$\gamma_{xy} \approx \tan\alpha \cong \alpha = \frac{\Delta S}{2L} \qquad [2.3]$$

The magnitude of stress is then given by

$$\sigma_{xy} = E\gamma_{xy} \qquad [2.4]$$

where E is Young's modulus of silicon.

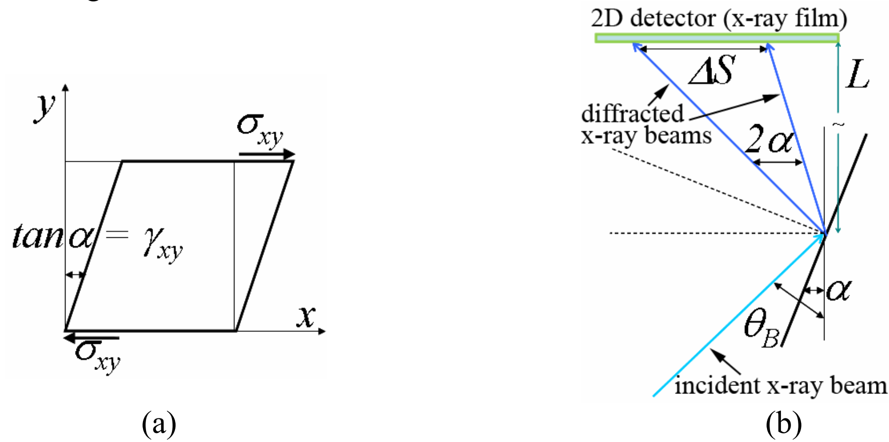

Figure 28. (a) Tilting of lattice planes due to simple shear; (b) Orientation contrast due to tilt (Note: Magnitude of angle α with respect to the Bragg angle θ_B is exaggerated. $\alpha << \theta_B$. Also the sample-film distance L is very large (~ 300mm) compared to ΔS).

2.3.3.1 Shear strain/stress mapping procedure

The following formulae were used to calculate shear strain and shear stress:

$$\gamma_{xy} = \Delta S / 2L \qquad [2.3]$$
$$\sigma_{xy} = E\gamma_{xy} \qquad [2.4]$$

ΔS is the resulted shift of the diffracted spot from the tilting of the plane normal due to its strain
L is the Specimen-to-Film distance ~ **20 cm (Wafer), 35 cm (Brick)**
E is the Elastic Modulus of Silicon = **160 GPa**

*How **ΔS** (in cm) was measured*
We have used Adobe Photoshop to:
1. Superimpose images of X-ray reticulographs to obtain a large grain or selecting separate grains in the reticulograph that are well defined.

2. Measured **ΔS** using a "Reference Grid" (Shown in Figure 29) – With the large grain that was being analyzed, a region of **0** strain was selected to measure the displacement of the shift where present. The notation of measuring distortion is illustrated in figure 30.

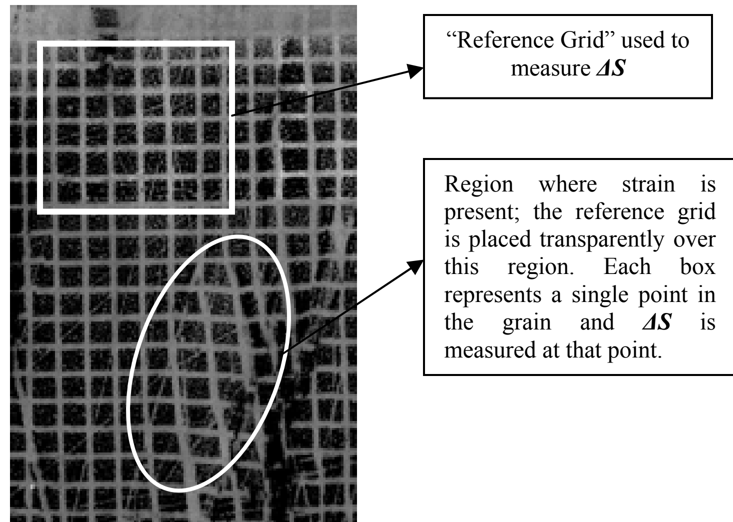

Figure 29. X-ray Reticulograph taken from one section of Face 4.

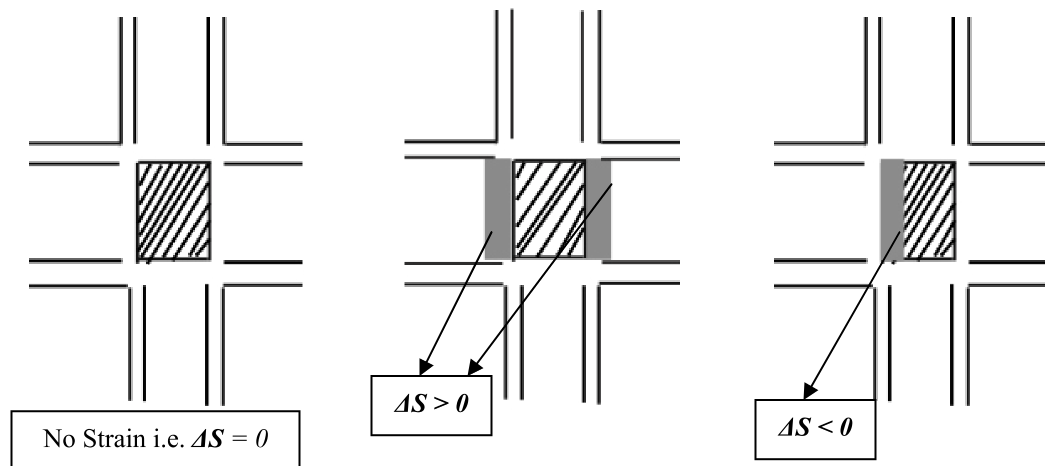

Figure 30. Schematic and notation of measuring distortion

2.4 Results & Discussion

2.4.1 SWBXR of Brick Faces

Stress measurements have been carried out on 4 faces in reflection geometry, which is able to image up to a depth of approximately 10 microns below the surface. Figure 31 illustrates a schematic of a brick sample denoting the different faces and their relationship to the growth direction.

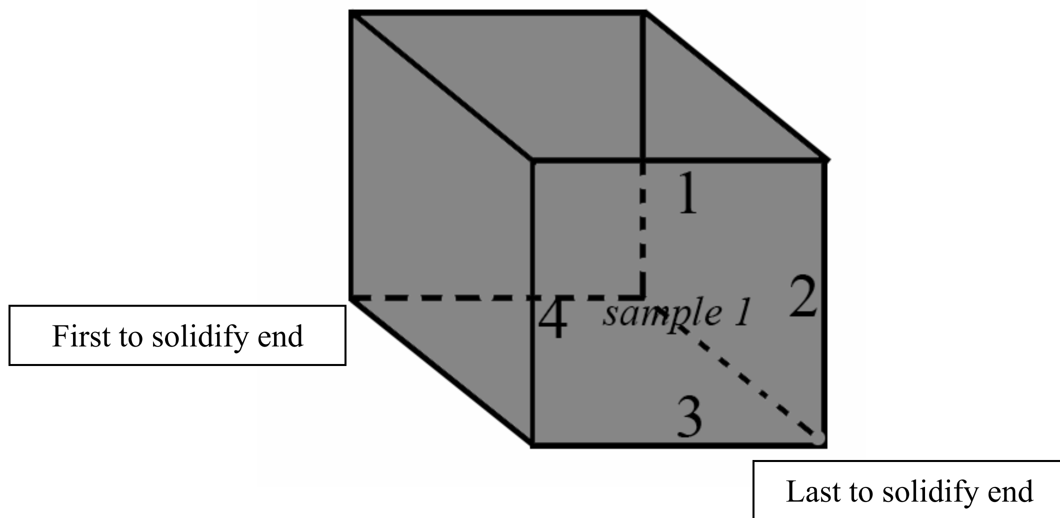

Figure 31. Schematic of brick sample

Images of the faces assembled topographs shown in figure 32 reveal variety of multiple large grains which are partially or completely strained. Figure 33 shows the stress mapping of the 4 faces.

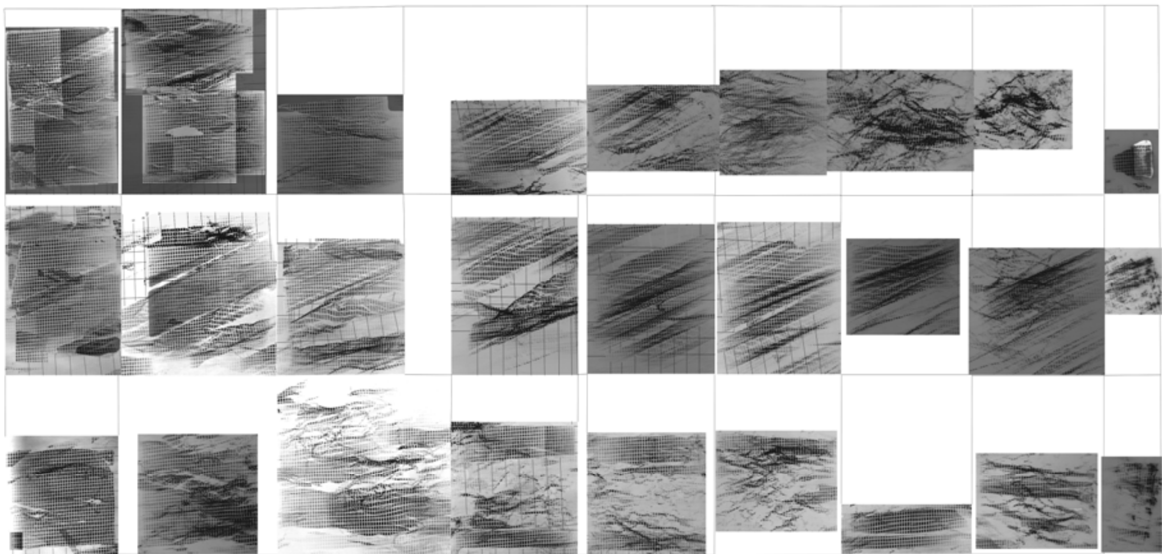
(a) Face 1

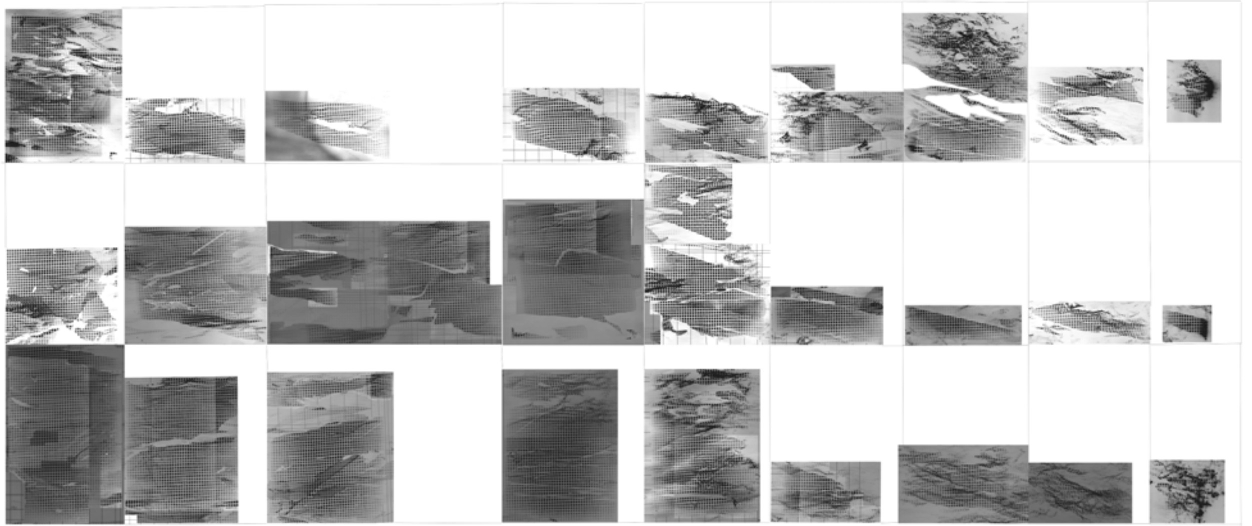

(b) Face 2

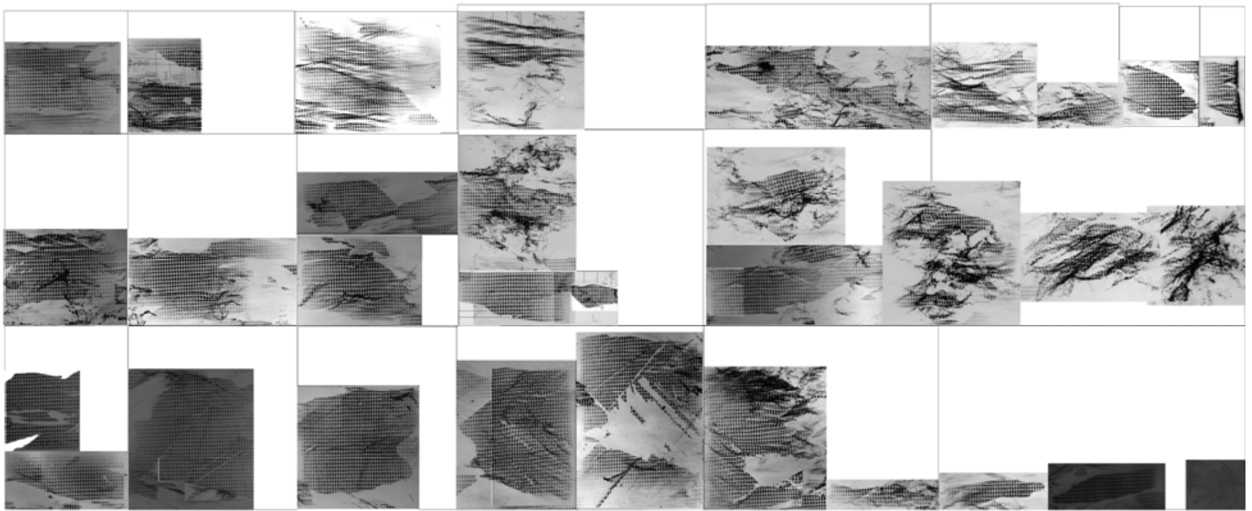

(c) Face 3

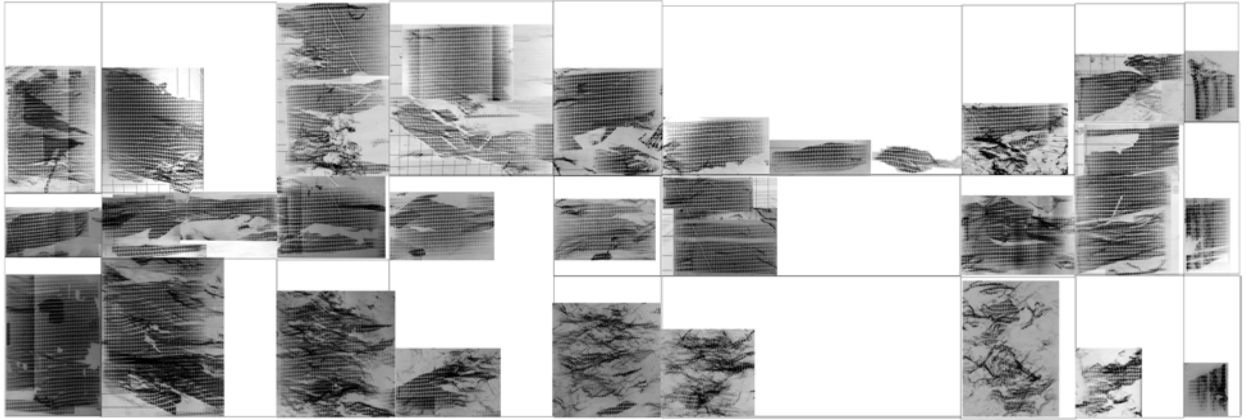

(d) Face 4

Figure 32. X-ray images of the four faces of mc-Si brick assembled from reticulographs of various grains. *Note*: First-to-solidify end is to the left and the last-to-solidify end is to the right in each figure.

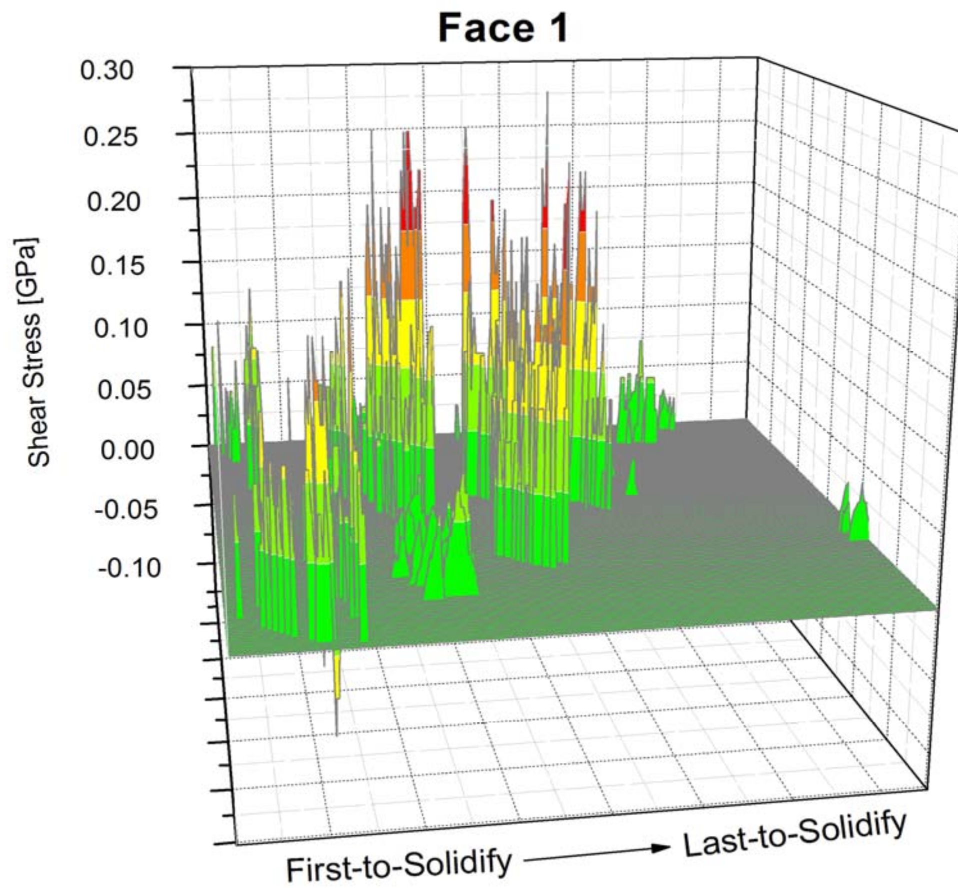

(a)

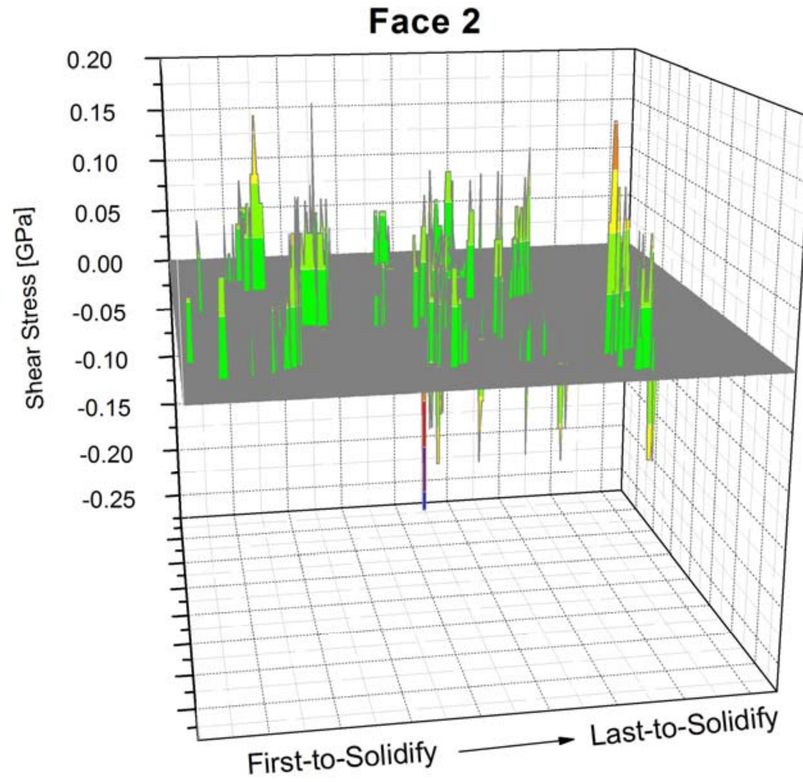

(b)

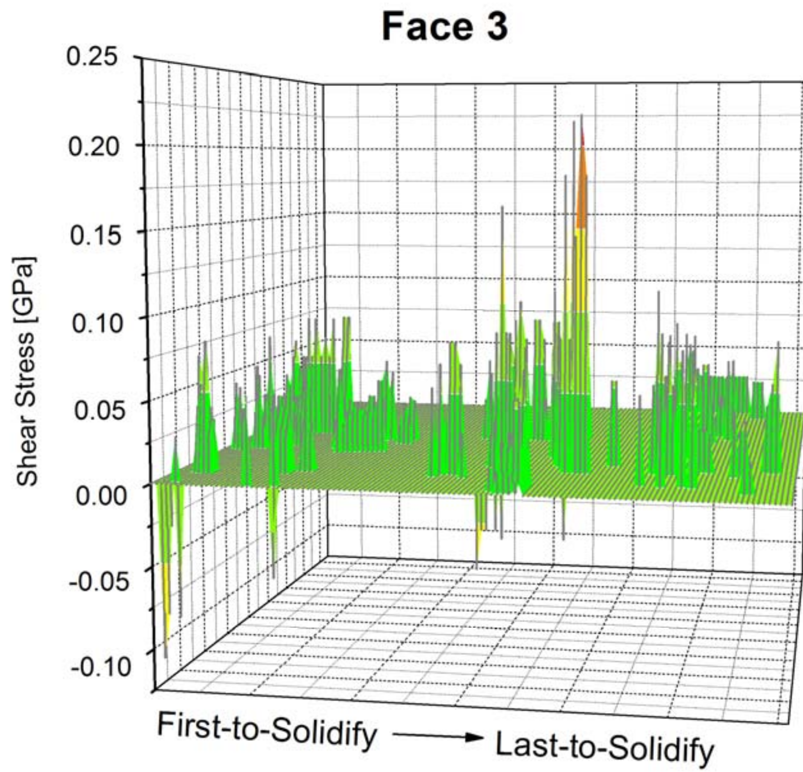

(c)

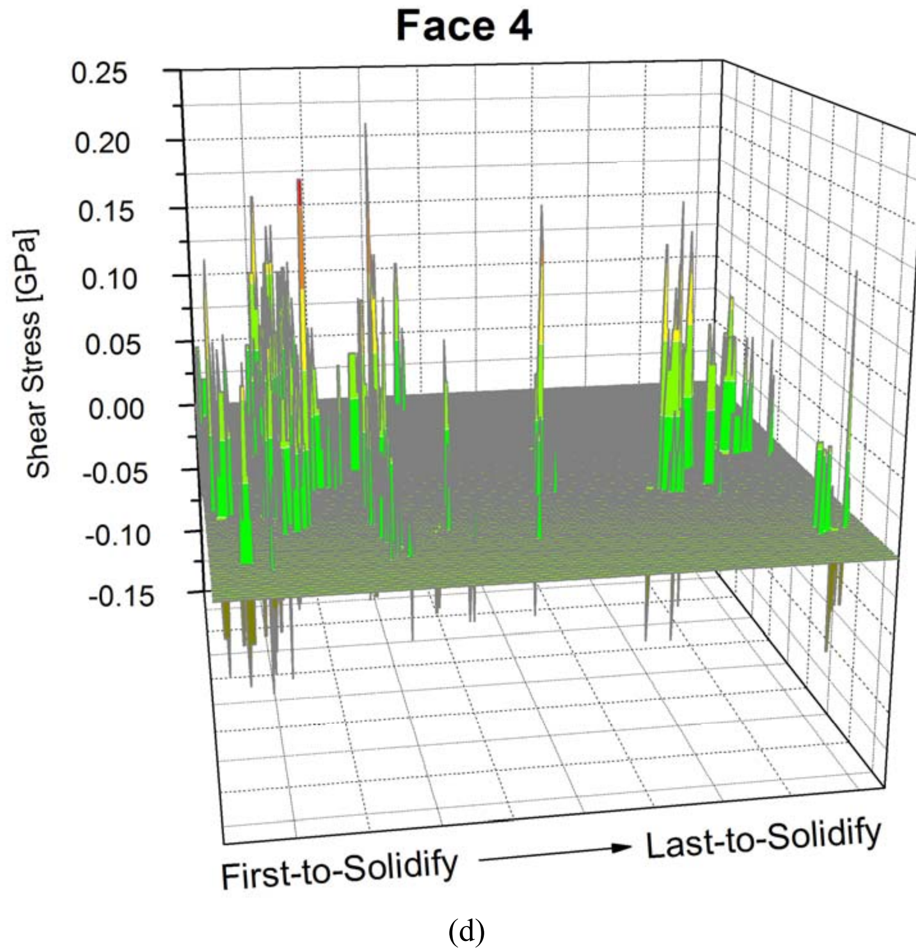

(d)

Figure 33. Stress map of four faces of the mc-Si brick sample from the corresponding reticulographs in figure 32.

The shear stress maps of the four faces indicate that the stress levels on the surface of the brick range from 0 to 0.25 GPa. Higher stress levels are found at the first-to-solidify end of both faces 1 and 4. The last-to-solidify end of faces 2 and 3 indicate to have high stress levels.

The variations of stress levels on the band sawed brick could be attributed to the growth process and more specifically to the non-uniform post growth cooling arising to temperature gradients in the furnace. Cutting the bricks using the band saw does not appear to introduce significant stress levels on the surface of the bricks.

2.4.2 SWBXR of Wafers

Wafers from the brick were sliced by using wire-saws. These wafers were then subjected to subsequent processing for solar cell fabrication. The processing stages of each wafer studied are described in table 3.

Table 3. List of wafers studied

Wafer Type	Processing stage
Clean	Clean
NaOH Etch	Clean + NaOH etch
Diffusion	Clean + NaOH etch + Diffusion
Print	Clean + NaOH etch + Diffusion + Print

Figure 34 shows optical photographs of the 4 wafers clearly showing the grain microstructure. The wafers are single crystals with a straight line grain boundary near edge 3. A region of small grains that are slightly misoriented from the rest of the wafer is also observed at this grain boundary. The (220) reflection was used to record transmission topographs (i.e. reticulographs in this case) for each wafer using a 1 mm mesh to determine its stress levels. Stress values calculated from the distortion of the mesh was mapped across each wafer. Figure 35 shows the X-ray reticulographs recorded from the 4 wafers and its corresponding shear stress maps.

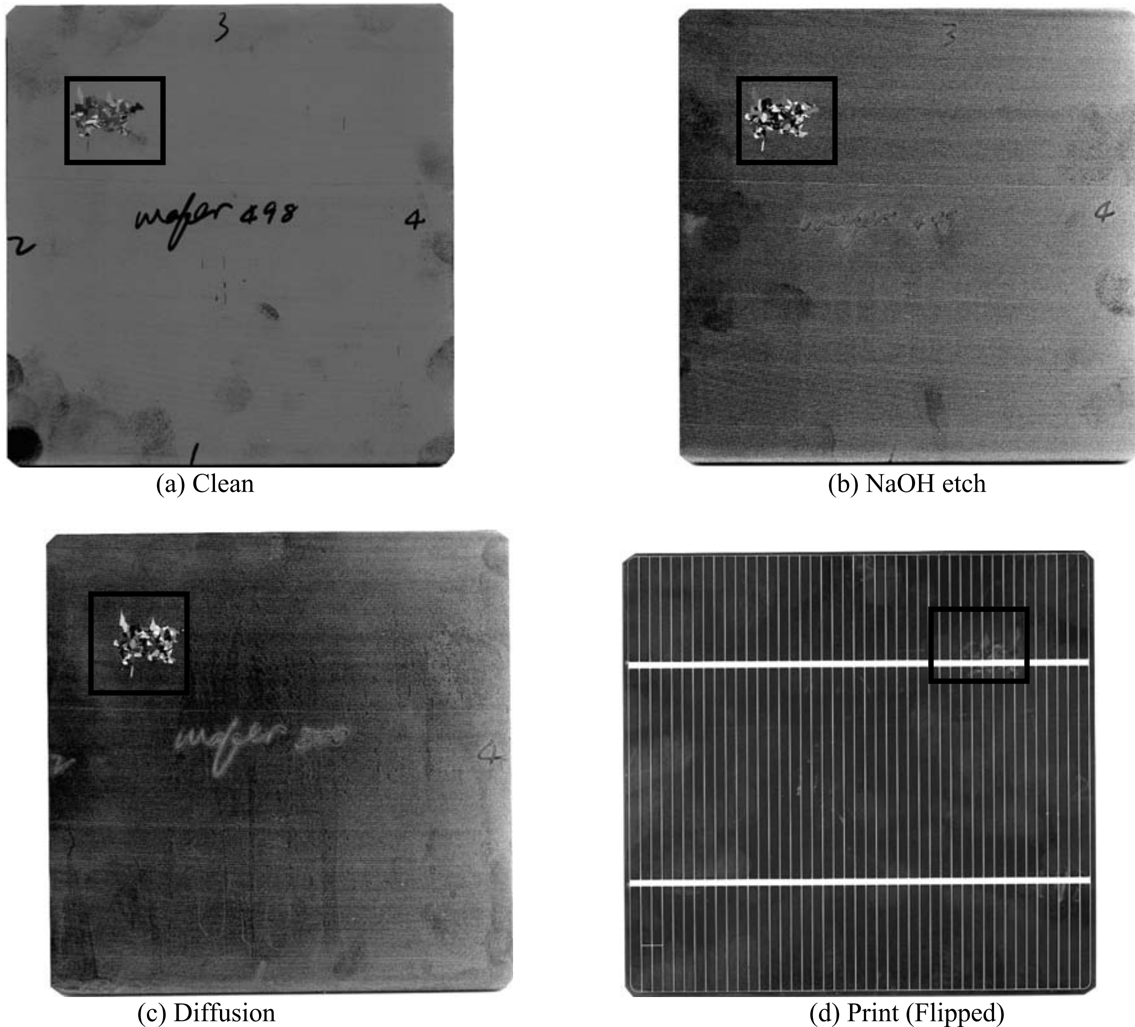

(a) Clean (b) NaOH etch (c) Diffusion (d) Print (Flipped)

Figure 34. Optical photographs of wafers sliced from the brick sample and processed to different stages of the solar cell fabrication. Black rectangle denotes region containing small grains. These grains are slightly misoriented with respect to main wafer orientation.

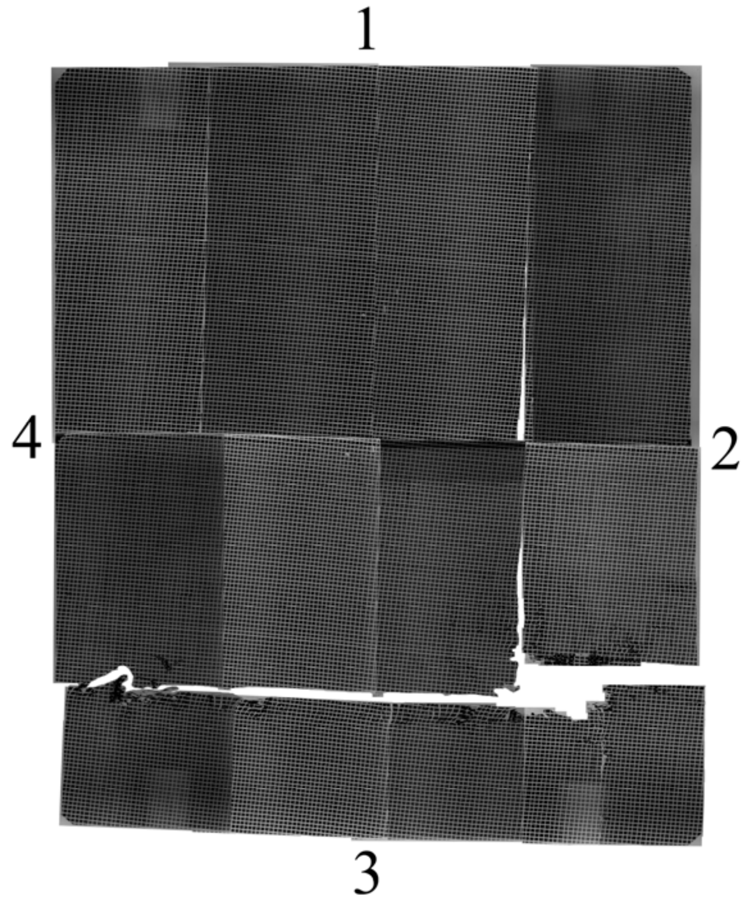

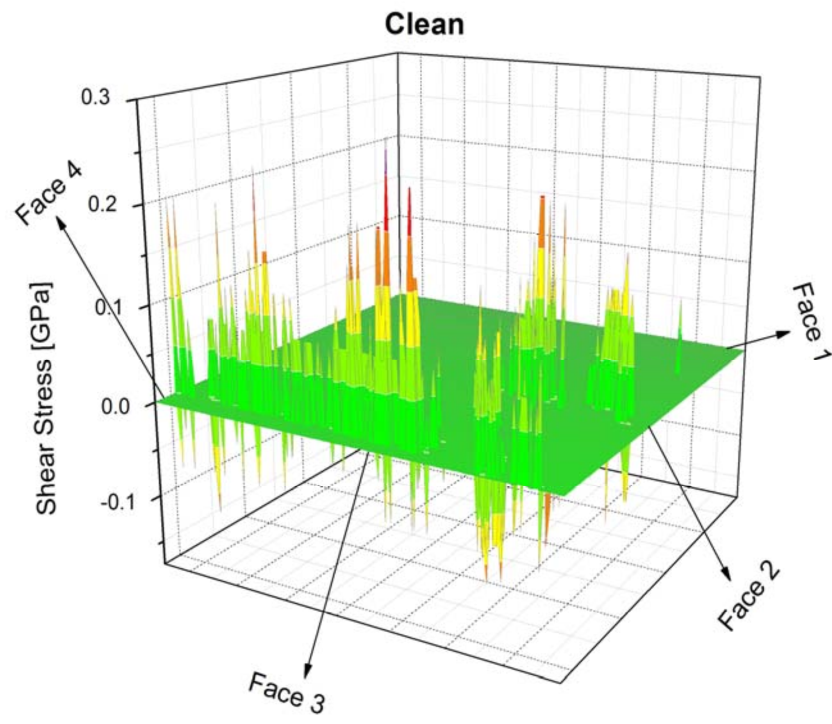

(a) Clean

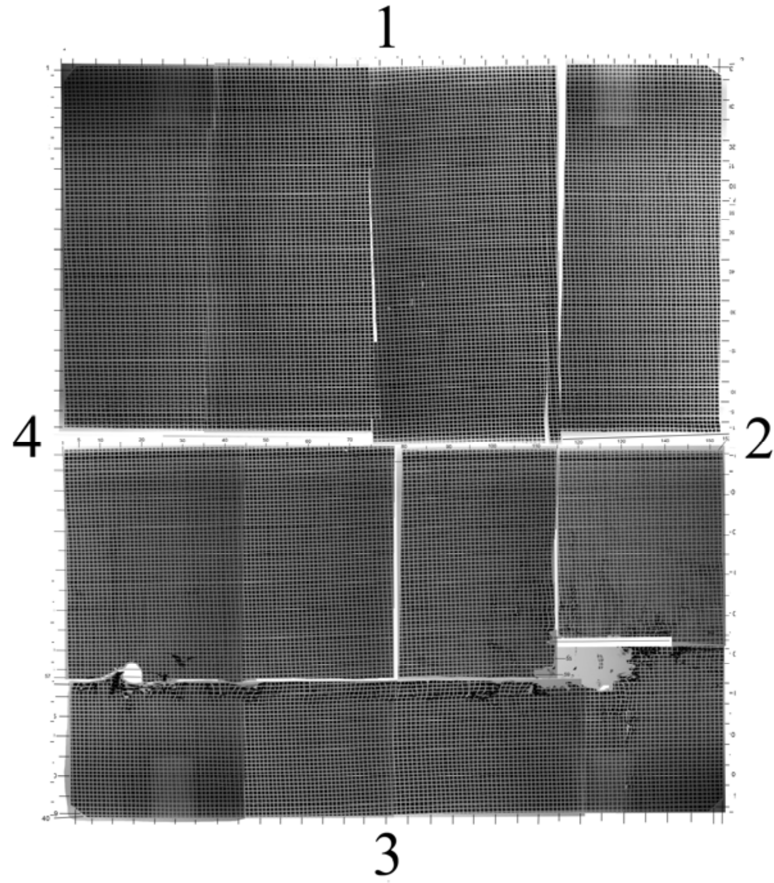

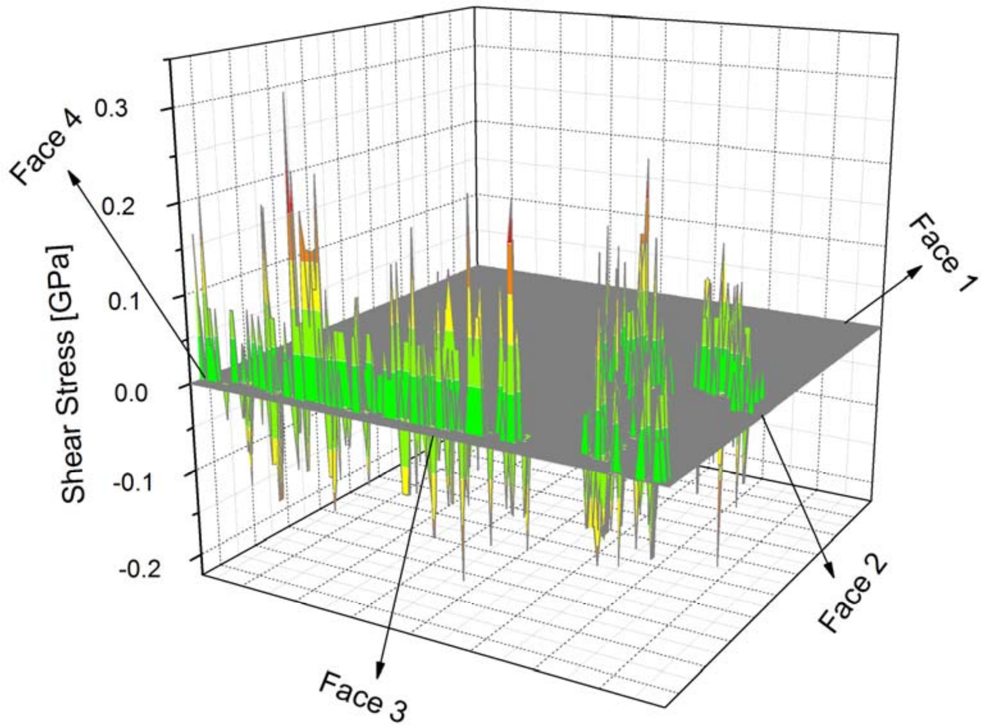

(b) NaOH Etch

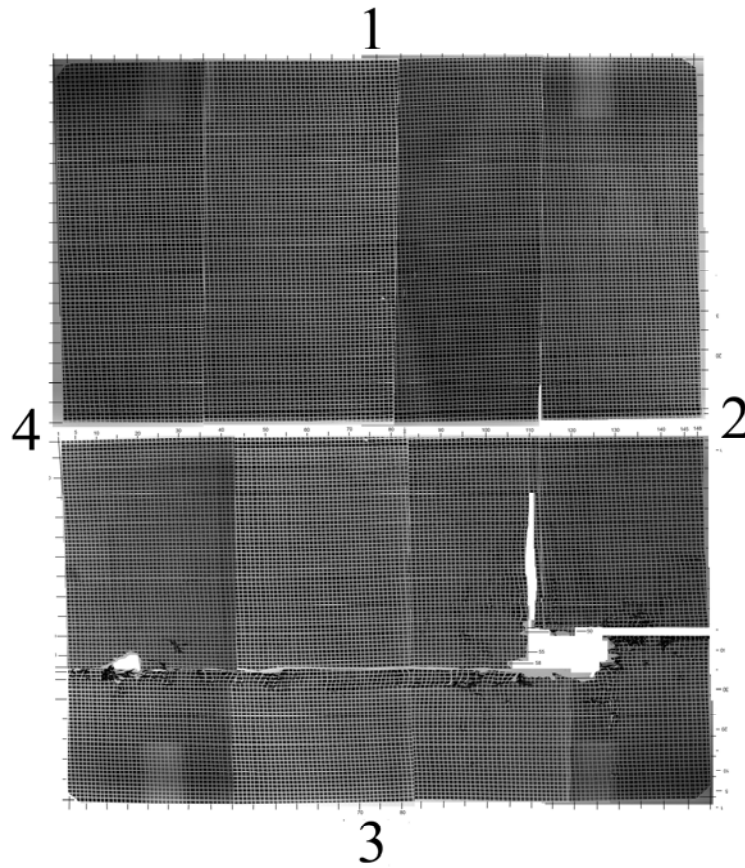

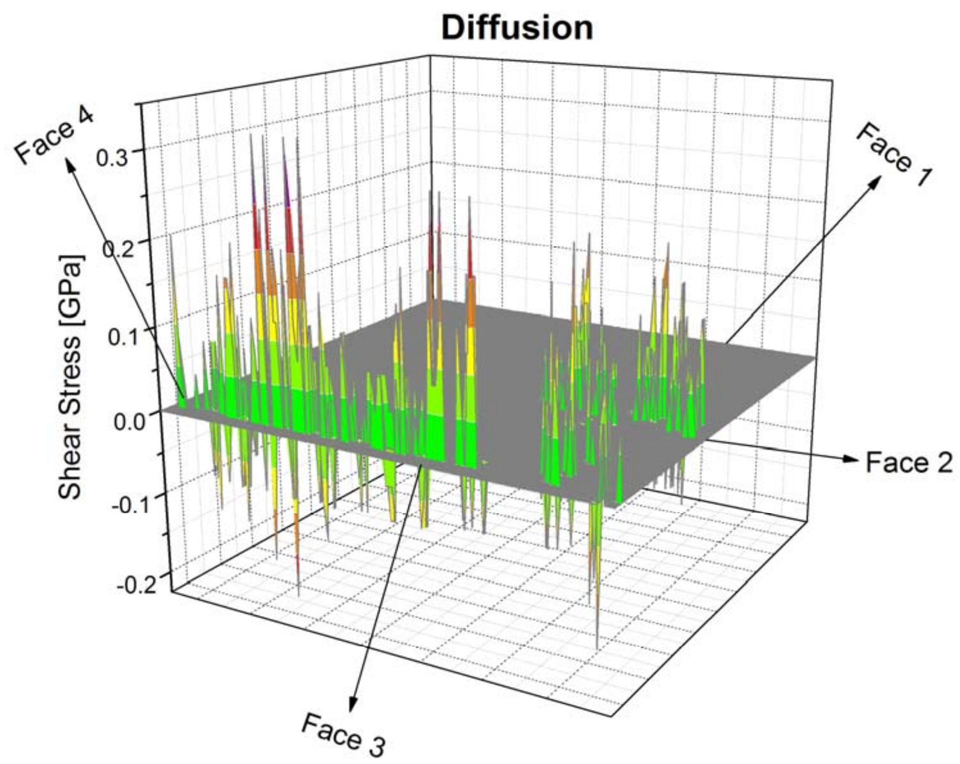

(c) Diffusion

Figure 35. X-ray reticulographs and its corresponding stress maps of wafers sliced from the brick sample and processed to different stages of the solar cell fabrication.

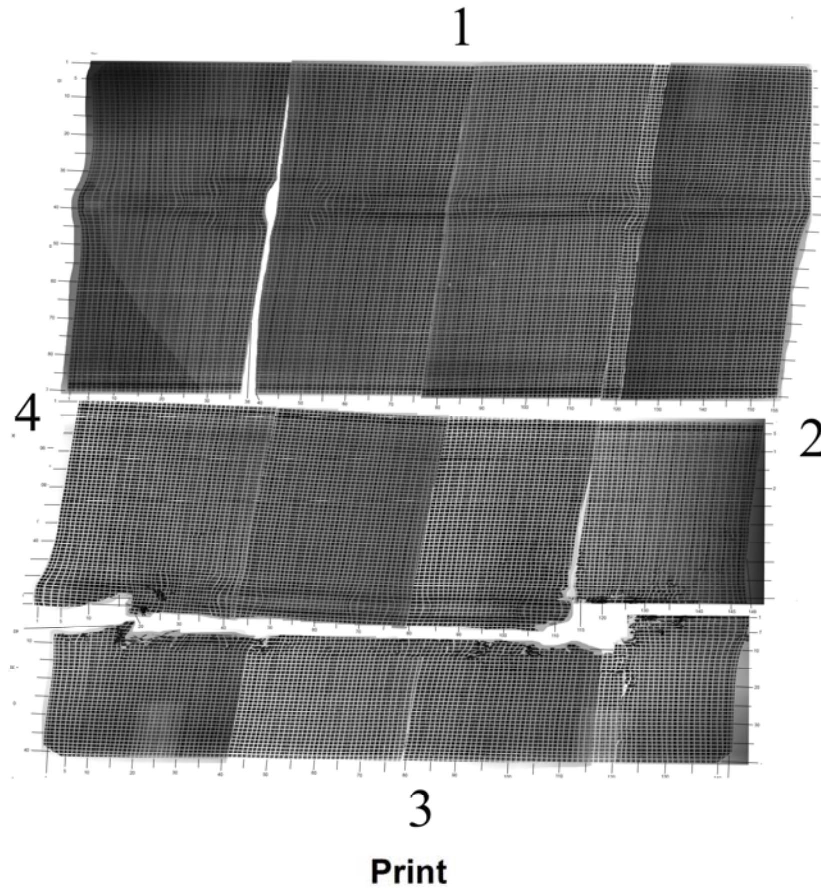

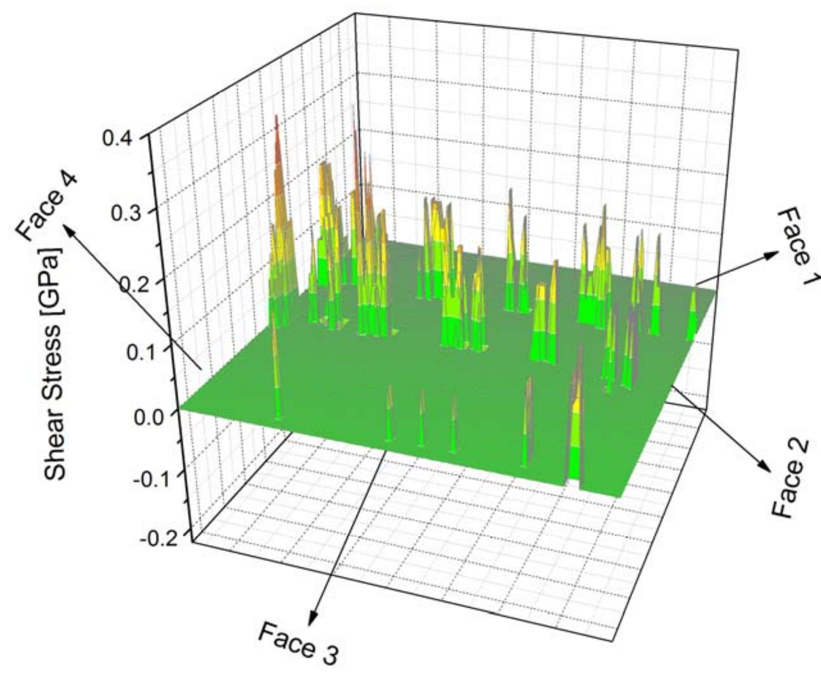

(d) Print

Figure 35. X-ray reticulographs and its corresponding stress maps of wafers sliced from the brick sample and processed to different stages of the solar cell fabrication.

As shown in figure 35, the stress levels vary from 0 to 0.3 GPa across the wafers as the edges are nearly stress-free indicated by the essentially undistorted mesh. The wafers are more or less strain-free except for high stress levels observed adjacent to a straight grain boundary running near the edge corresponding to face 3. In the case of the print wafer (figure 35(d)), high stress levels are observed at several points across the wafer, which correspond to the locations of the depositing of metallic contacts. The difference of expansion coefficients[33] between silicon and the metallic contact could lead to the generation of stress in the wafer.

The variations of shear stress caused in these wafers are likely due to the wire sawing near the grain boundary where there are small grains being slightly misoriented with respect to the wafer. This stress will still exist regardless if it is processed in an etching step. As we discussed previously for the print wafer, the difference of expansion coefficients causes stress in the wafer, this could likely be avoided by selecting a metal that has a similar thermal expansion and also does not readily oxidize.

2.4 Conclusion

The grain structure, strain level and dislocation content of the band-sawed mc-Si and wire-sliced wafers from the brick processed for solar cell fabrication are characterized by synchrotron X-ray topography. Quantitative measurements of shear stress were extracted using synchrotron X-ray reticulography. The following observations were observed: (1) the brick had higher stress levels at the first-to-solidify end of both faces 1 and 4 whereas faces 2 and 3 indicate to have high stress levels at the last-to-solidify end which is likely caused by non-uniform cooling; and (2) wafers having high stress levels observed adjacent to a straight grain boundary running near the edge corresponding to face 3 and, high stress levels appearing at several points across the print wafer corresponding to the locations of the depositing of metallic contacts are likely caused by the differences of thermal expansion between the metallic contact and Si.

3. Conclusions

I) Various methods were used to attempt low temperature growth of GaN nanostructures by thermal CVD. The morphology and crystal structure have been characterized using SEM, EDX, and TEM.

GaN nanopowders were synthesized through the reaction between gallium (Ga) atoms from the decomposition of gallium acetylacetonate and ammonia (NH_3) gas molecules at temperatures as low as 500 ^oC without a catalyst and as low as 400 ^oC using a Ni catalyst. These are the lowest temperatures reported for GaN synthesis so far.

Nanoneedles were observed as low as 450 ^oC with a 75 sccm NH_3 flow rate and chamber pressure of 15 torr whereas nanopowders was evident with 100 sccm flow rate with pressures ranging from 20 to 200 torr. The type of fluid flow (e.g. turbulent or laminar) that is undergoing in the reaction zone could likely influence the type of morphology obtained on the BN substrate. The ammonia molecules do not adsorb readily on the surface as a result and the growth of nanoneedles is preferred when the flow is laminar[27].

Nanoneedles that were grown non-catalytically were observed to have partial edge dislocations. High densities of nanoneedles were observed when using UV assisted radiation, the diameters ranged from 10 ~ 30 nm whereas non-catalytically, the diameter was 58 nm. It is also possible that the self-catalyzed VLS mechanism is not taking place since the alloy droplet of the nanoneedles grown from the BN facet was not observed. The method of using powdered Ga mixed with CaF_2 resulted in no yield of GaN in which the temperature was not sufficient to initiate the liquid alloy droplet required to grow nanostructures.

II) The grain structure, strain level and dislocation content of band sawed mc-Si brick and wire-sliced wafers (and its subsequent processing for solar cell fabrication) are studied by using synchrotron white beam X-ray topography (SWBXT). Quantitative information on shear stress is obtained by employing the technique of synchrotron white beam X-ray reticulography (SWBXR).

Based on the stress analysis, the following observations were observed: (1) the brick had higher stress levels at the first-to-solidify end of both faces 1 and 4 whereas faces 2 and 3 indicate to have high stress levels at the last-to-solidify end which is likely caused by non-uniform cooling; and (2) wafers having high stress levels observed adjacent to a straight grain boundary running near the edge corresponding to face 3 and, high stress levels appearing at several points across the print wafer corresponding to the locations of the depositing of metallic contacts are likely caused by the differences of thermal expansion between the metallic contact and Si.

Appendix - Chemical & Physical Properties of Gallium Acetylacetonate

Gallium (III) acetylacetonate, $Ga(CH_3COCHCOCH_3)_3$ (or its shorthand notation $Ga(acac)_3$) is an organometallic complex having a decomposition temperature of 196 ^oC. The mean Ga-O bond length is 1.90 Å and table 3 shows the bond lengths and angles, values were obtained using Chem3D 11.0 software. The six oxygen atoms from the three acetylacetonate bidentate ligands shape a near octahedral structure[40] which is bonded to the Ga atom as indicated by the molecule illustrated in figure 36.

Table 4. Bond lengths & angles of gallium (III) acetylacetonate

	Bond Length [Å]		Bond Angle [º]		Bond Angle [º]
O(10)-Ga(8)	1.900	O(10)-Ga(8)-O(1)	172.4	C(22)-C(21)-O(17)	131.7
O(2)-Ga(8)	1.900	O(17)-Ga(8)-O(2)	168.9	C(4)-C(3)-O(1)	130.8
O(1)-Ga(8)	1.911	O(9)-Ga(8)-O(16)	165.7	C(15)-C(14)-O(10)	130.6
Ga(8)-O(9)	1.910	Ga(8)-O(10)-C(14)	159.4	C(19)-C(18)-O(16)	129.7
Ga(8)-O(16)	1.911	Ga(8)-O(17)-C(21)	157.1	C(12)-C(11)-O(9)	129.5
O(17)-C(21)	1.219	Ga(8)-O(2)-C(6)	155.0	C(7)-C(6)-O(2)	129.8
O(16)-C(18)	1.383	Ga(8)-O(16)-C(18)	126.0	C(5)-C(3)-O(1)	115.1
O(10)-C(14)	1.220	Ga(8)-O(9)-C(11)	127.4	C(13)-C(11)-O(9)	115.8
O(9)-C(11)	1.383	Ga(8)-O(1)-C(3)	122.5	C(20)-C(18)-O(16)	115.3
O(2)-C(6)	1.219	O(2)-Ga(8)-O(10)	99.1	C(19)-C(21)-O(17)	105.0
O(1)-C(3)	1.383	O(1)-Ga(8)-O(9)	97.1	C(12)-C(14)-O(10)	104.4
C(21)-C(22)	1.502	O(2)-Ga(8)-O(16)	97.7	C(4)-C(6)-O(2)	104.3
C(19)-C(21)	1.472	O(2)-Ga(8)-O(9)	95.2	C(7)-C(6)-C(4)	125.8
C(18)-C(20)	1.505	O(10)-Ga(8)-O(16)	96.3	C(15)-C(14)-C(12)	124.9
C(18)-C(19)	1.359	O(17)-Ga(8)-O(9)	92.7	C(22)-C(21)-C(19)	123.3
C(14)-C(15)	1.501	O(1)-Ga(8)-O(16)	91.3	C(6)-C(4)-C(3)	120.4
C(12)-C(14)	1.472	O(17)-Ga(8)-O(1)	91.7	C(21)-C(19)-C(18)	117.9
C(11)-C(13)	1.505	O(17)-Ga(8)-O(10)	90.4	C(14)-C(12)-C(11)	117.6
C(11)-C(12)	1.359	O(2)-Ga(8)-O(1)	79.6	C(20)-C(18)-C(19)	114.8
C(6)-C(7)	1.501	O(10)-Ga(8)-O(9)	75.5	C(13)-C(11)-C(12)	114.5
C(4)-C(6)	1.472	O(17)-Ga(8)-O(16)	75.4	C(5)-C(3)-C(4)	114.1
C(3)-C(5)	1.505				
C(3)-C(4)	1.359				

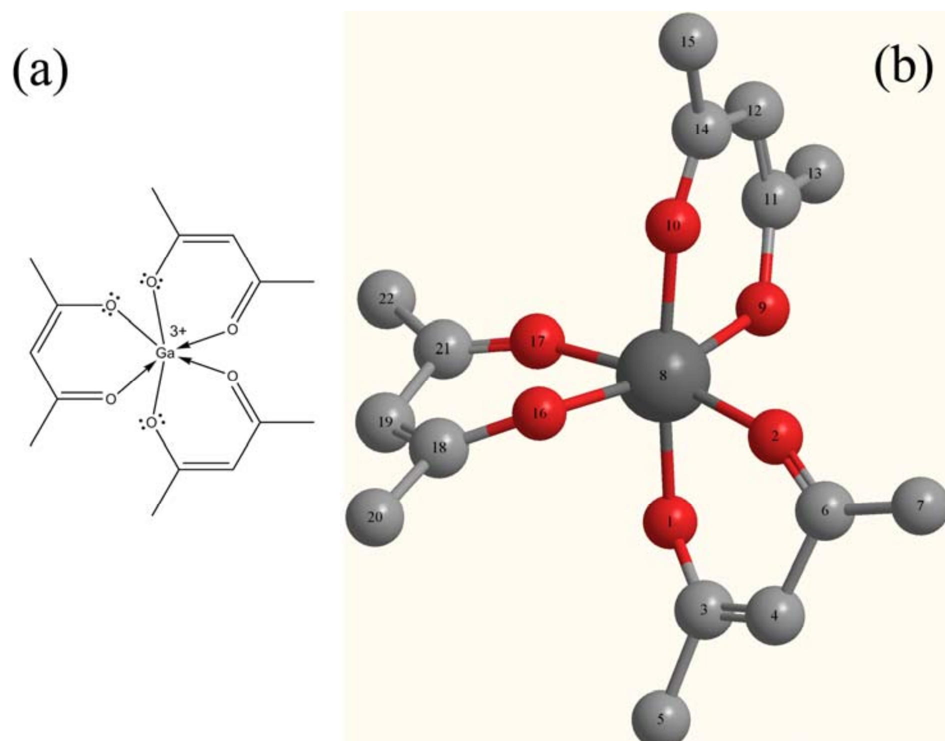

Figure 36. Line structure (a) and (b) the ball and stick model of Ga(acac)$_3$ showing its atomic numbering.

At[41] 298K, the molar enthalpy of combustion of Ga(acac)$_3$ is 7963 kJ mol^{-1} and dissociation energy of the Ga-O bond is 156 kJ mol^{-1}.

References

[1] C. J. Humphreys, MRS Bull. **33**(4), 464 (2008)
[2] N.W. Ashcroft, N.D. Mermin, *Solid State Physics*, p. 567 (Thomson Learning, 1976)
[3] H. Morkoç, S. Strite, J. Vac. Sci. Technol. B **10**(4), 1237 (1992)
[4] T. Lei, T.D. Moustakas, R.J. Graham, Y. He, S.J. Berkowitz, J. Appl. Phys. **71**(10), 4933 (1992)
[5] S.S. Liu, D.A. Stevenson, J. Electrochem. Soc. **125**(7), 1161-1162 (1978)
[6] R. Groh, G. Gerey, L. Bartha, J.I. Pankove, Phys. Stat. Sol. A **26**, 353 (1974)
[7] J. Unland, B. Onderka, A. Davydov, R. Schmid-Fetzer, J. Cryst. Growth. **256**, 33 (2003)
[8] J. Zhang, L. Zhang, J. Vac. Sci. Technol. B **21**(6), 2415 (2003)
[9] A.D. Walsh, P.A. Warsop, Trans. Faraday Soc. **57**, 345 (1961)
[10] E. O. Wiig, G.B. Kistiakowsky, J. Am. Chem. Soc. **54**, 1806 (1932)
[11] D. Chrysostomou, J. Flowers, F. Zaera, Surf. Sci. **439**, 34 (1999)
[12] K. Tamaru, K. Tanaka, S. Fukasaku, S. Ishida, Trans. Faraday Soc. **61**, 765 (1965)
[13] N. Dietz, M. Strassburg, V. Woods, J. Vac. Sci. Technol. A **23**(4), 1221 (2005)
[14] H. Amano, N. Sawaki, I. Akasaki, Y. Toyoda, Appl. Phys. Lett. **48**(5), 353 (1986)
[15] V. Dmitriev, K. Irvine, G. Bulman, J. Edmond, A. Zubrilov, V. Nikolev, I. Nikitina, D. Tsvetkov, A. Babanin, A. Sitnikova, Y. Musikhin, N. Bert, J. Cryst. Growth **166**, 601 (1996)
[16] M. Law, J. Goldberger, P. Yang, Annu. Rev. Mater. Res. **34**, 83 (2004)
[17] K.W. Chang, J.J. Wu, J. Phys. Chem. B **106**, 7796 (2002)
[18] Z. C. Feng, *III-Nitride Semiconductor Materials*, p.370 (Imperial College Press, Danvers, MA, 2006)
[19] F. Cerrina, C. Marrian, MRS Bull. **21**(12), pp. 56-57, 59 (1996)
[20] H.J. Fan, P. Werner, M. Zacharias, Small **2**(6), 701 (2006)
[21] M. He, P. Zhou, S. Mohammed, G. Harris, J. Halpern, R. Jacobs, W. Sarney, L. Salamanca-Riba, J. Cryst. Growth **231**, 358 (2001)
[22] R.S Wagner, W.C. Ellis, Appl. Phys. Lett. **4**, 89-90 (1964)
[23] J. Gröbner, R. Wenzel, G.G. Fischer, R. Schmid-Fetzer, J. Phase. Equil. **20**(6), 615 (1999)
[24] M. He, I. Minus, P. Zhou, S. Mohammed, J. Halpern, R. Jacobs, W. Sarney, L. Salamanca-Riba, R.D. Dispute, Appl. Phys. Lett. **77**, 3731 (2000)
[25] M. He, P. Zhou, S. Mohammed, G. Harris, J. Halpern, R. Jacobs, W. Sarney, L. Salamanca-Riba, J. Cryst. Growth **231**, 358 (2001)
[26] A. M. S. ElAhl, M. He, P. Zhou, G. Harris, L. Salamanca-Riba, F. Felt, H. Shaw, A. Sharma, M. Jah, D. Lakins, T.Steiner, S. Mohammed, J. Appl. Phys. **94**, 7749 (2003)
[27] S. Mohammed, J. Chem. Phys. **125**, 094705-1 (2006)
[28] J.J. Carvajal, N. Gomez, J. Bai, M. Dudley, J. C. Rojo, Proc. SPIE 6121, 61210E-2 (2006)
[29] S. Mohammed, J. Chem. Phys. **127**, 244702-1 (2007)
[30] B. Gil, *Group III nitride semiconductor compounds* (Oxford Science Publications, Oxford, 1998)
[31] A. Slaoui, R.T. Collins, MRS Bull. **32**(3), 211 (2007)
[32] H.J. Möller, C. Funke, M. Rinio, S. Scholz, Thin Sol. Films **487**, 179 (2005)

---

[33] P. Panek, M. Lipinski, E. Beltowska-Leman, K. Drabczyk, R. Ciach, Opto-electron. Rev. **11**(4), 269 (2003)

[34] S.M. Sze, *Physics of Semiconductor Devices*, *2nd Ed.*, pp. 64-65 (John Wiley & Sons, 1981)

[35] C.J. Frosch, L. Derick, J. Electrochem. Soc. **104**, 547 (1957)

[36] B.S. Richards, J.E. Cotter, C.B. Honsberg, and S.R. Wenham, Proc. IEEE **28**, 375 (2000)

[37] B. Raghothamachar, G. Dhanaraj, J. Bai, M. Dudley, Microsc. Res. Tech. **69**(5), 343 (2006)

[38] B.K. Tanner, *X-ray Diffraction Topography*, pp. 81-96 (Pergamon Press, Inc., 1976)

[39] A.R. Lang, A.P.W. Makepeace, J. Phys. D: Appl. Phys. **32**, A97 (1999)

[40] K. Dymock, G.J. Palenik, Acta Cryst. B **30**, 1364 (1974)

[41] K.J. Cavell, G. Pilcher, J. Chem. Soc., Faraday Trans. 1, **73**, 1590 (1977)